

Prediction of polymer extension, drag reduction, and vortex interaction in direct numerical simulation of turbulent channel flows ^F

Cite as: Phys. Fluids **34**, 073318 (2022); <https://doi.org/10.1063/5.0094978>

Submitted: 07 April 2022 • Accepted: 29 June 2022 • Accepted Manuscript Online: 30 June 2022 • Published Online: 20 July 2022

Published open access through an agreement with University of Leeds

 L. F. Mortimer and M. Fairweather

COLLECTIONS

 This paper was selected as Featured



View Online



Export Citation



CrossMark

ARTICLES YOU MAY BE INTERESTED IN

[A new boundary layer integral method based on the universal velocity profile](#)

Physics of Fluids **34**, 075130 (2022); <https://doi.org/10.1063/5.0100367>

[Numerical simulations of cell sorting through inertial microfluidics](#)

Physics of Fluids **34**, 072009 (2022); <https://doi.org/10.1063/5.0096543>

[On the origin of mode B instability of the wake of a square cylinder](#)

Physics of Fluids **34**, 074116 (2022); <https://doi.org/10.1063/5.0101403>



Physics of Fluids

Special Topic: Paint and Coating Physics

Submit Today!

Prediction of polymer extension, drag reduction, and vortex interaction in direct numerical simulation of turbulent channel flows

Cite as: Phys. Fluids **34**, 073318 (2022); doi: [10.1063/5.0094978](https://doi.org/10.1063/5.0094978)

Submitted: 7 April 2022 · Accepted: 29 June 2022 ·

Published Online: 20 July 2022



View Online



Export Citation



CrossMark

L. F. Mortimer^{a)}  and M. Fairweather

AFFILIATIONS

School of Chemical and Process Engineering, University of Leeds, Leeds LS2 9JT, United Kingdom

^{a)} Author to whom correspondence should be addressed: l.f.mortimer@leeds.ac.uk

ABSTRACT

Hydrodynamic and viscoelastic interactions between the turbulent fluid within a channel at $Re_\tau = 180$ and a polymeric phase are investigated numerically using a multiscale hybrid approach. Direct numerical simulations are performed to predict the continuous phase and Brownian dynamics simulations using the finitely extensible nonlinear elastic dumbbell approach are carried out to model the trajectories of polymer extension vectors within the flow, using parallel computations to achieve reasonable computation timeframes on large-scale flows. Upon validating the polymeric configuration solver against theoretical predictions in equilibrium conditions, with excellent agreement observed, the distributions of velocity gradient tensor components are analyzed throughout the channel flow wall-normal regions. Impact on polymer stretching is discussed, with streamwise extension dominant close to the wall, and wall-normal extension driven by high streamwise gradients of wall-normal velocity. In this case, it is shown that chains already possessing high wall-normal extensions may attempt to orientate more in the streamwise direction, causing a curling effect. These effects are observed in instantaneous snapshots of polymer extension, and the effects of the bulk Weissenberg number show that increased We_B leads to more stretched configurations and more streamwise orientated conformities close to the wall, whereas, in the bulk flow and log-law regions, the polymers tend to trace fluid turbulence structures. Chain orientation angles are also considered, with We_B demonstrating little influence on the isotropic distributions in the log-law and bulk flow regions. Polymer–fluid coupling is implemented through a polymer contribution to the viscoelastic stress tensor. The effect of the polymer relaxation time on the turbulent drag reduction is discussed, with greater Weissenberg numbers leading to more impactful reduction. Finally, the velocity gradient tensor invariants are calculated for the drag-reduced flows, with polymers having a significant impact on the Q–R phase diagrams, with the presence of polymers narrowing the range of R values in the wall regions and causing flow structures to become more two-dimensional.

© 2022 Author(s). All article content, except where otherwise noted, is licensed under a Creative Commons Attribution (CC BY) license (<http://creativecommons.org/licenses/by/4.0/>). <https://doi.org/10.1063/5.0094978>

I. INTRODUCTION

Remarkable effects are observed upon the addition of low concentrations of high-molecular-weight polymer additives to both single-phase and multiphase flow systems. Upon historical observation of this behavior in straight pipes (Toms, 1948), subsequent investigations into such systems indicate two major mechanisms: alteration of flow instabilities (Azaiez and Homsy, 1994a; Azaiez and Homsy, 1994b; Kumar and Homsy, 1999; Sureshkumar, 2001; Sadanandan and Sureshkumar, 2002; Fouxon and Lebedev, 2003; Dubief *et al.*, 2013; Garg *et al.*, 2018) and induced turbulent drag reduction (DR) (Lumley, 1969; Nieuwstadt and Den Toonder, 2001; Sher and Hetsroni, 2008; Berman, 1978; Xi, 2019; Gu *et al.*, 2020; Lumley, 1977). Mechanisms through which turbulence suppression and drag

reduction can be instigated in wall-bounded flows are of interest to many industries. Practically, systems which would benefit from turbulence control via overcoming the pressure loss associated with skin-friction drag (Choi *et al.*, 1994) are an ideal complement for the injection of polymer additives. Even with low $O(10)$ ppm (Lumley, 1973), the inclusion of dispersed linear chain polymers has been shown to drastically reduce the frictional drag. Depending on the mechanical properties of the polymer species, drag reductions relative to Newtonian flows have been observed as high as 80% (Virk, 1975). The benefits of such drag reduction mechanisms have been exploited within many industries over the last half-century, including vastly improving the performance of oil transport (Yusuf *et al.*, 2012) and hosing in fire-fighting (Figueredo and Sabadini, 2003). Polymeric flows

are also of interest to industries dealing with inertial particle transport, such as water treatment (Edomwonyi-Otu and Adelakun, 2018) and nuclear waste processing (Lockwood *et al.*, 2021) due to their ability to flocculate and settle particulates through electrochemical and hydrophobic interactions between the phases. In the latter case, more efficient, well-understood, and economic transport methods are paramount to ensuring the implementation of effective and safe process designs for waste management.

Upon initial discovery, many experimental studies were performed in the hope of determining the underpinning physics surrounding the dynamics responsible for these useful features. Early findings indicated that DR effects were primarily caused by the coupling between the continuous turbulent phase and the polymer extension and conformity dynamics, with the most effective DR obtained through the use of long linear flexible-chain species (Virk, 1975). It should be noted here that despite various polymer-solvent pairs being used in experimental studies, the onset of DR seems to depend mostly on the mechanical properties of the polymer (along with the Newtonian flow properties). Polyethylene oxide (PEO) and polyacrylamide (PAM) are, in general, the most commonly used species for experimental studies of DR effects in concentrations of O(10) to O(100) wppm (Owolabi *et al.*, 2017; Lumley, 1969; Virk, 1975; Xi, 2019).

A particular grey area in the field relates to the way in which polymers interact with turbulent structures present in wall-bounded flows, which is important for elucidating and, hence, predicting bulk-scale dynamics accurately and across industrial timeframes. The near-wall region (around $y^+ = 15$), in particular, was observed to be initially affected upon injection of polymers, and attempts at linking DR mechanisms to turbulent burst events in these regions were made in early experimental and theoretical studies (Gordon and Balakrishnan, 1972; Peterlin, 1970). When subject to turbulence in the near-wall region, polymer chains interact with the fluid fluctuations, and drag reduction commences within the plane of peak turbulence energy. Many early studies indicated that polymers and other drag-reducing additives modify the nature of the turbulent structures within this region (Oldaker and Tiederman, 1977; Tiederman *et al.*, 1985; Blackwelder and Kaplan, 1976; Stone and Graham, 2003; Hetsroni *et al.*, 1997). Another important observation made is that polymers are capable of redirecting energy between various time- and length scales (White and Mungal, 2008), subsequently modifying the velocity fluctuations and providing a greatly altered flow through which a secondary phase, such as a particulate or droplet phase, may need to be advected. Recent studies of such flows indicate that the coherent turbulent structures close to the wall lead to increased streamwise turbulence intensities, whereas cross-stream components are reduced (Ilg *et al.*, 2002; Xi and Graham, 2010). Experimental studies also indicated that polymeric flow systems can be described based on a single viscosity coefficient as well as a time constant relating to the relaxation time of the polymer (Seyer and Metzner, 1969; Metzner, 1977). Throughout these early studies, polymer-induced drag reduction mechanisms were partitioned into two schools of thought. The first relates to viscous theory (Lumley, 1969), wherein polymers are stretched by turbulence causing an increase in the effective viscosity in local regions of the flow. This mainly takes place in the buffer layer where turbulence fluctuations are then suppressed. This leads to an increase in the buffer layer thickness, and the wall friction is, therefore, reduced (Benzi *et al.*, 2004). In contrast, the elastic theory (Tabor and De Gennes, 1986)

considers the comparison of elastic energy stored in the polymer chain to the kinetic energy in the buffer region. Because the viscoelastic length scale is larger than the flow Kolmogorov length scale, conventional energy cascade mechanisms are inhibited, and so, the buffer layer thickens (Li *et al.*, 2015; Thais *et al.*, 2013).

In order to better address the fundamental dynamics of polymer-fluid interaction on scales unresolvable by experimental methods, various computational tools have been developed in recent years capable of modeling such processes. Since the direct numerical simulation (DNS) work of Sureshkumar *et al.* (1997), various attempts at modeling the polymeric phase have been attempted to provide much more detail and resolution of both the flow and polymer conformation fields. In most models, polymer molecules are represented and treated as elastic dumbbells (two beads connected together with a nonlinear spring), giving rise to the finitely extensible nonlinear elastic (FENE) model (Bird *et al.*, 1987). In such models, the ideal chain representation is employed which ignores nonbonded interactions between intermediate chain sections such as those arising from van der Waals and electrostatic forces. Individual polymer chains within the solution are also considered as sufficiently far apart that their collisions can be neglected. In most computational studies, to reduce further complexity, a continuum approach to the polymer conformation tensor field is often taken via the Peterlin approximation (Bird *et al.*, 1987), which closes the constitutive equations for the time evolution of the conformation tensor at a given flow position and relies upon knowledge of the mean polymer extension within that local region. Early simulations performed using this technique obtained a very good qualitative agreement with similar experiments. In studies of the effect of polymers on viscoelastic turbulent flows, the streamwise vorticity fluctuations were observed to decrease and the low-speed streaks within the buffer layer were less densely populated (Sureshkumar *et al.*, 1997). DR characteristics have been shown to be parameterized by three key properties (Gupta *et al.*, 2004): the bulk Reynolds number of the continuous phase, Re_B ; the Weissenberg number, We_e , quantifying the ratio of the polymer relaxation time to the friction flow scale; and the extensibility parameter, b , quantifying the maximum extensibility of the polymer chain. The polymer conformation and, hence, coupled effects also vary depending on the flow region, as the morphology of turbulence structures varies with wall distance. Progress toward understanding the notion of maximum drag reduction (MDR), where system parameters such as polymer concentration no longer offer beneficial improvements to drag reduction, was made by Li *et al.* (2015). They demonstrated that the MDR asymptote occurs when the ratio of the convective time scale associated with streamwise vorticity fluctuations and the vortex rotation timescale is approximately equal.

Although DR is observed when using the Peterlin approximation, resolution and detail surrounding the specific orientations of polymer chains are lost, which means that we are unable to study the effect of polymer orientation and interaction with the local flow structures on the dynamics and mechanisms which lead to DR. Other alternate models also fall short, with Oldroyd-B models are incapable of accurately predicting polymers with high Weissenberg numbers and Giesekus models only evolve the stress tensor, meaning information surrounding the polymer conformation state is unavailable. Despite the standard FENE method being computationally intensive, modern high-performance parallel computation allows calculations to be

performed in reasonable timeframes. The benefit of increased fidelity means that these processes can be considered in much greater detail. In this study, therefore, DNS and the FENE polymer simulation method are employed in order to more closely study the trajectories of polymer conformation under the influence of various near-wall coherent turbulence structures.

II. METHODOLOGY

A. Direct numerical simulation

The simulations presented in this article represent polymers which are dispersed within and transported throughout fully developed turbulent channel flows. We assume the carrier phase to be a continuum, incompressible and a viscoelastic fluid which is modeled within an orthogonal Cartesian domain. The continuous phase dynamics for the motion of the fluid are governed by the following conservation equations for mass and momentum, given as follows:

$$\nabla \cdot \mathbf{u} = 0, \quad (1)$$

$$\frac{\partial \mathbf{u}}{\partial t} + \mathbf{u} \cdot \nabla \mathbf{u} = -\frac{\nabla p}{\rho_F} + \beta \nu_0 \nabla^2 \mathbf{u} + (1 - \beta) \frac{\nu_0}{\mu_{p0}} \nabla \cdot \mathbf{T} + \mathbf{f}_{PG}. \quad (2)$$

Here, $\mathbf{u}(\mathbf{x}, t)$ is the fluid velocity vector at Cartesian position vector \mathbf{x} , t is the time, p is the fluid pressure, ρ_F is the fluid phase density, β is the ratio of solvent (μ_s) to the total zero-shear rate viscosity (ν_0), μ_{p0} is the polymer contribution to the total zero-shear solution viscosity, and \mathbf{T} is the viscoelastic contribution to the total stress tensor. As in previous work, we may non-dimensionalize the above equations using bulk flow units to obtain

$$\nabla \cdot \mathbf{u}^* = 0, \quad (3)$$

$$\frac{\partial \mathbf{u}^*}{\partial t^*} + \mathbf{u}^* \cdot \nabla \mathbf{u}^* = -\nabla p^* + \frac{\beta}{Re_B} \nabla^2 \mathbf{u}^* + \frac{(1 - \beta)}{\beta Re_B} \nabla \cdot \mathbf{T}^* + \mathbf{f}_{PG}. \quad (4)$$

Here, $\mathbf{u}^* = \mathbf{u}/U_B$, $t^* = tU_B/\delta$, $p^* = p/\rho_F U_B$ and $\mathbf{T}^* = \mathbf{T}/(\mu_{p0} U_B^2/\nu_0)$ with U_B the bulk velocity of the Newtonian flow and δ the channel half-height. Finally, $Re_B = \frac{U_B \delta}{\nu_0}$ is the bulk Reynolds number of the Newtonian flow. The mean flow direction is chosen to be in the positive x^* direction, hence the pressure gradient term takes the form $\mathbf{f}_{PG} = (Re_\tau/Re_B)^2 \hat{\mathbf{e}}_x^*$ with $\hat{\mathbf{e}}_x^*$ a unit vector aligned with the streamwise direction. Here, Re_τ is the equivalent shear Reynolds number with $Re_\tau = 180$ for all cases presented in this study. The domain boundaries are $(-7, 7)$ in x^* , $(-1, 1)$ in y^* , and $(-3, 3)$ in z^* with limits enforcing periodic conditions in the streamwise and spanwise directions (x^* and z^*), and no-slip wall boundaries in the wall-normal direction (y^*). The above equations are solved using Nek5000 (Fischer et al., 2008), an efficient highly parallel direct numerical simulation code widely used in academia and industry. The software employs the spectral element method developed by Patera (1984) and unites the geometric flexibility of the finite element method with the excellent numerical stability and accuracy of spectral methods. The domain is discretized into $27 \times 18 \times 23$ hexahedral elements, upon which the solution to Eqs. (3) and (4) is represented as a tensor-product of seventh-order Lagrange polynomials at each of the Gauss-Lobatto-Legendre (GLL) nodes. For comparison with finite volume or finite difference techniques, this is approximately equivalent to 4×10^6 grid points. Further details for the Newtonian single-phase channel flow calculations can be found in our previous work (Mortimer et al., 2019). In this work, both Newtonian

flows (where we ignore the non-Newtonian effects and focus purely on the influence of the fluid on polymer conformation) and non-Newtonian flows (where the polymer contribution to the viscoelastic stress tensor is explicitly calculated) are considered.

B. Calculation of the additional viscoelastic stress tensor

Assuming knowledge of the viscoelastic contribution to the stress tensor, \mathbf{T}^* , at each GLL node, non-Newtonian DNS calculations can be performed. In addition to Eqs. (3) and (4), the system is supplemented by FENE simulations within each unique GLL cell in order to represent the polymer dynamics. The calculation of polymer extension trajectories is necessary to couple the local polymer conformation to the additional viscoelastic stress tensor, \mathbf{T}^* . In order to do so, Brownian dynamics simulations are performed (detailed in Sec. II C). For a given GLL cell in the simulation, N_{POL} polymer dumbbells are simulated, each with end-to-end extension vector \mathbf{Q} which is made dimensionless using $\sqrt{k_B T/H^*}$. Here, k_B is the Boltzmann constant, T is the temperature, and H^* is the Hookean spring constant. From the ensemble of N_{POL} \mathbf{Q} vectors, the polymer conformation tensor can be obtained as $\mathbf{c} = \langle \mathbf{Q}\mathbf{Q} \rangle$. The viscoelastic stress tensor \mathbf{T}^* can then be determined using

$$\mathbf{T}^* = \frac{f\mathbf{c} - \mathbf{1}}{We_B}. \quad (5)$$

Here, $\mathbf{1}$ is the equilibrium unit isotropic tensor state, and We_B is the bulk Weissenberg number, which is the ratio of the polymer relaxation time, λ , to the bulk fluid timescale δ/U_B , i.e., $We_B = \lambda U_B/\delta$. The function f is the Peterlin function (Peterlin, 1970) determined as

$$f = \frac{L^2 - 3}{L^2 - tr(\mathbf{c})}. \quad (6)$$

Here, L^2 is the square of the dimensionless maximum extensibility, such that $tr(\mathbf{c}) \leq L^2$, and is made dimensionless identically to \mathbf{c} .

C. Brownian dynamics simulations using the FENE dumbbell model

The simulations reported in this study use the FENE dumbbell model to predict trajectories of the end-to-end extension vector \mathbf{Q} . The connector vector satisfies the stochastic differential equation (Öttinger, 2012) as follows:

$$d\mathbf{Q}(t) = \left[\boldsymbol{\kappa}(t) \cdot \mathbf{Q}(t) - \frac{1}{2We_B} \mathbf{F}_C \right] dt + \frac{1}{\sqrt{We_B}} d\mathbf{W}(t). \quad (7)$$

Here, $\boldsymbol{\kappa} = \nabla \mathbf{u}^{*T}$ is the velocity gradient tensor transpose and $d\mathbf{W}(t)$ is the three-dimensional stochastic Wiener process with mean and variance $(0, dt)$ representing Brownian motion due to thermal noise experienced by the polymer chain. \mathbf{F}_C is the dimensionless spring force, given by

$$\mathbf{F}_C = \frac{\mathbf{Q}}{\left(1 - \frac{Q^2}{b}\right)}, \quad (8)$$

where \sqrt{b} is the dimensionless maximum extensibility. To numerically integrate Eq. (7), we use a two-step semi-implicit predictor-corrector

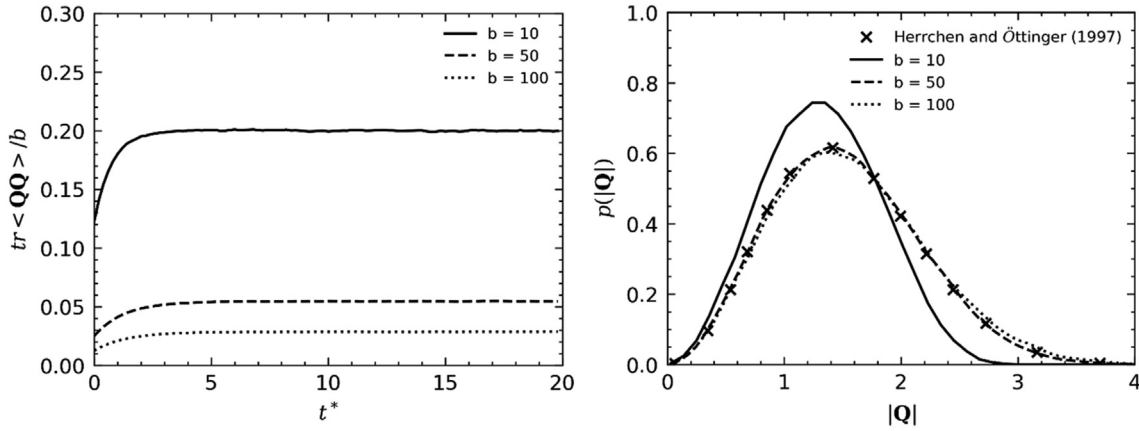


FIG. 1. Temporal evolution of $tr \langle \mathbf{Q}\mathbf{Q} \rangle / b$ in equilibrium conditions (left) and probability distribution of polymer extension $|\mathbf{Q}|$ with comparison against the $b = 50$ FENE results of Herrchen and Öttinger (1997) (right).

scheme (Öttinger, 2012; Gupta et al., 2004). To perform a single time-step for an extension vector \mathbf{Q} , we calculate the predictor step

$$\bar{\mathbf{Q}}_{N+1} = \mathbf{Q}_N + \left[\boldsymbol{\kappa}_N^* \cdot \mathbf{Q}_N - \frac{1}{2We_B} \mathbf{F}_{C,N} \right] \delta t^* + \frac{1}{\sqrt{We_B}} d\mathbf{W}(t)_N, \quad (9)$$

followed by the corrector step:

$$\mathbf{Q}_{N+1} = \mathbf{Q}_N + \frac{1}{2} \left[\boldsymbol{\kappa}_{N+1}^* \cdot \bar{\mathbf{Q}}_{N+1} + \boldsymbol{\kappa}_N^* \cdot \mathbf{Q}_N \right] \delta t^* - \frac{1}{4We_B} \left[\bar{\mathbf{F}}_{C,N+1} + \mathbf{F}_{C,N} \right] \delta t^* + \frac{1}{\sqrt{We_B}} d\mathbf{W}(t)_N. \quad (10)$$

Here, the subscript N refers to the current step in the predictor-corrector process. The initial conditions for this process use the current extension vector and velocity gradient tensor. The corrector step is repeated until the predicted improvement satisfies an arbitrary error tolerance, chosen to be $\epsilon_{PC} = 1 \times 10^{-5}$ in the present simulations. The magnitude of the resulting vector \mathbf{Q}_{N+1} is then adjusted to satisfy the equation below, taking the one real root with magnitude less than

the maximum extensibility, \sqrt{b} , in order to avoid violated extension states and ensuring positive definiteness of the conformation tensor

$$|\mathbf{Q}|^3 - RHS |\mathbf{Q}|^2 - b \left(1 + \frac{\delta t^*}{4We_B} \right) |\mathbf{Q}| + b RHS = 0. \quad (11)$$

Equations (7)–(11) are solved on each unique GLL point before each fluid evolution calculation step takes place using a sub-timestep δt^* determined based on b and We_B . This is then, in effect, a multiscale simulation technique. The required number of sub-timesteps is investigated on a case-by-case basis to ensure the conformation tensor is statistically stationary.

III. RESULTS AND DISCUSSION

A. Newtonian dynamics in equilibrium conditions and polymer-laden turbulent channel flow at $Re_\tau = 180$

Simulations were first performed in equilibrium conditions, that is to say, under no fluid influence, equivalent to an infinite box where $u_F^* = 0$ everywhere. This is to accomplish two things: first, the

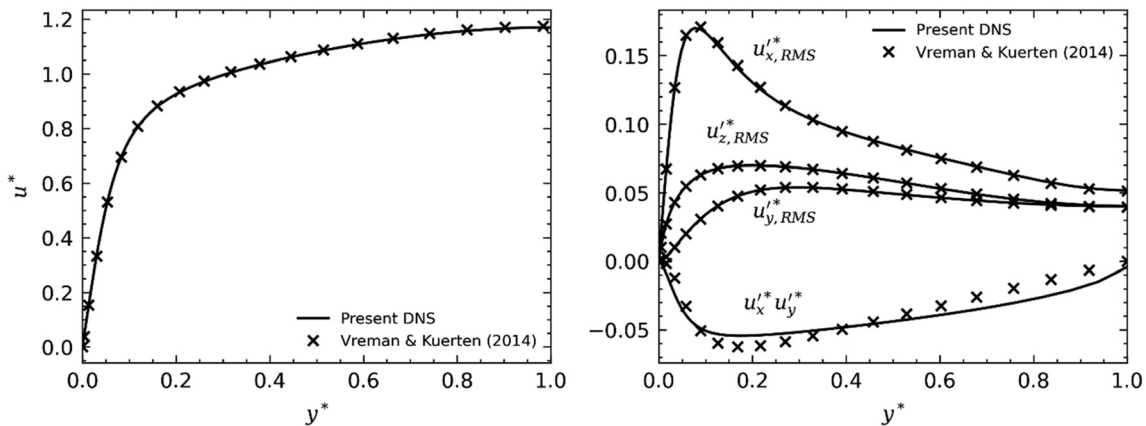


FIG. 2. Mean streamwise velocity u^* (left) and root mean square of velocity fluctuations $u_{d,RMS}^*$ with shear stress $u_x^* u_y^*$ (right) for fully developed turbulent channel flow at $Re_\tau = 180$. Results compared to the DNS database of Vreman and Kuerten (2014).

trajectory calculation technique must be validated, and second, the effect of the maximum extensibility parameter, b , on the settling time should be determined. Hundred polymers were injected with each component of their initial extensibilities chosen randomly between

-0.5 and 0.5 . These were then simulated for a total of $t^* = 20$ with constant time step $\delta t^* = 0.001$. The left plot in Fig. 1 illustrates the time evolution of the trace of the conformation tensor (normalized by b) for $b = 10, 50,$ and 100 , a typical range chosen to be similar to

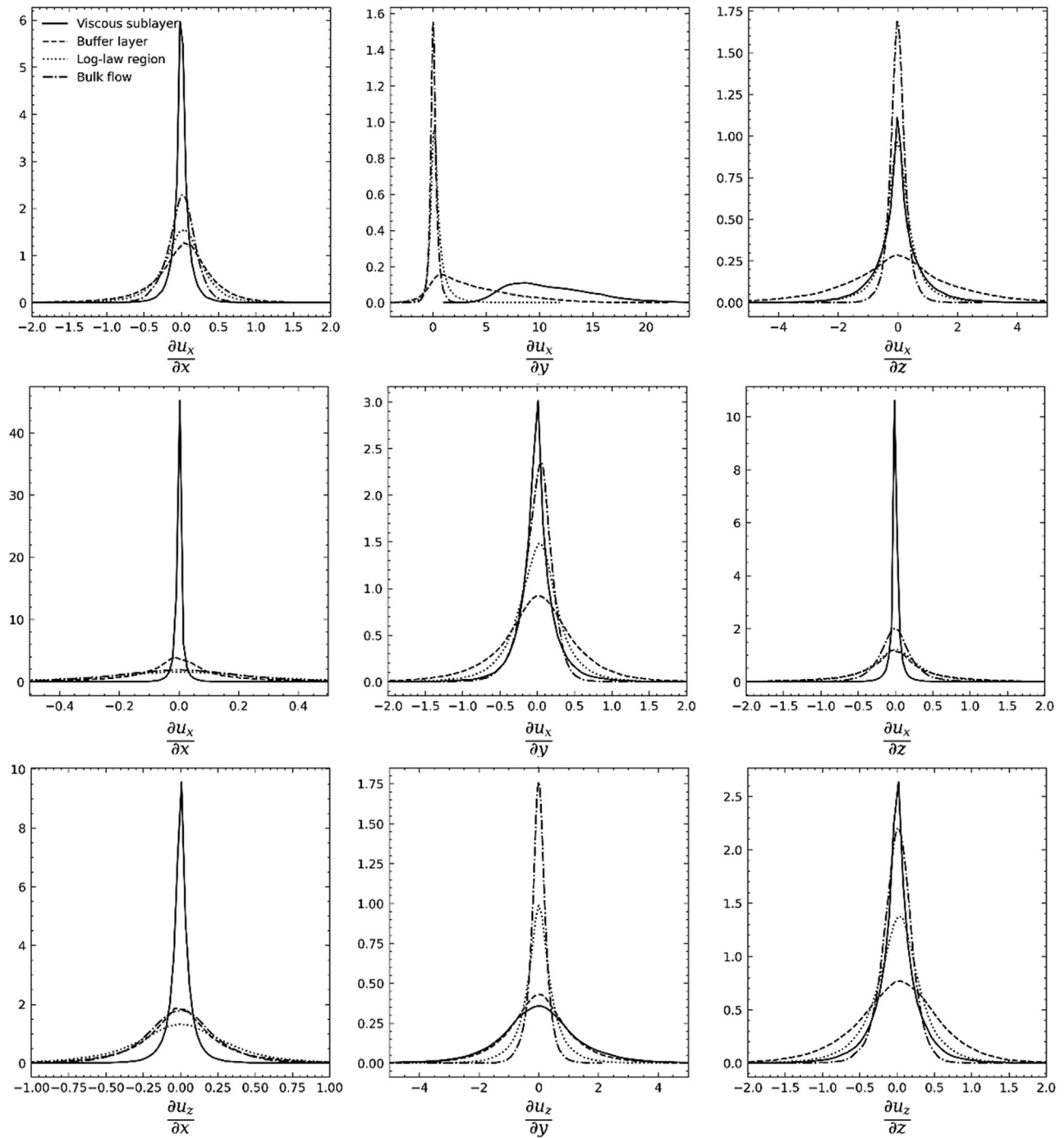


FIG. 3. Probability distribution function (PDF) of components of velocity gradient tensor for fully developed unladen turbulent channel flow at $Re_\tau = 180$. Regional dependence is illustrated.

TABLE I. Turbulent channel flow at $Re_\tau = 180$ wall-normal distance region classification.

Region	Distance from wall (*) (begins)	Distance from wall (*) (ends)
Bulk flow	0.200	1.000
Log-law region	0.166	0.200
Buffer layer	0.027	0.166
Viscous sublayer	0.000	0.027

those studied in both simulations and experiments in previous work (Gupta *et al.*, 2004; Teng *et al.*, 2018; Wedgewood and Öttinger, 1988). It is observed that the mean extension squared (relative to the maximum extension squared) reached equilibrium after $t^* = 5$ in all cases, with increased b exhibiting lower relative extensibilities as expected. The right plot in Fig. 1 demonstrates the probability distribution for a specific extension, $|\mathbf{Q}|$, sampled at $t^* = 20$. The results for $b = 50$ are compared to those obtained theoretically by Herrchen and Öttinger (1997) using the FENE radial equilibrium distribution function with excellent agreement obtained. Reducing the maximum extensibility parameter shifts the distribution to lower extensions, whereas doubling it has a very little effect. For this reason, $b = 50$ is chosen for the subsequent simulations performed under non-equilibrium conditions.

The simulations performed in the remainder of this study all take place within a turbulent channel flow, driven using a constant pressure gradient ensuring a bulk Reynolds number, $Re_B = 2800$, which corresponds to a shear Reynolds number, $Re_\tau = 180$. The details of the simulation setup and parameters for the Newtonian single-phase flow are found in Sec. II. The unladen continuous phase was simulated until the first- and second-order velocity field moments were statistically stationary, the results of which can be found in Fig. 2.

The left plot illustrates the mean streamwise velocity profile, with comparisons made to the DNS predictions of Vreman and Kuerten (2014). The right plot illustrates the three components of the root mean square of the velocity fluctuations as well as the main mean shear stress. In all cases, agreement with the validation data is at least

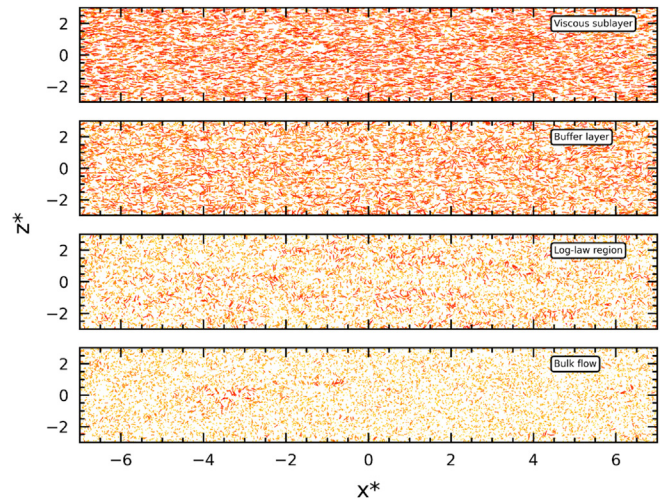


FIG. 4. Instantaneous polymer orientations for $b = 50$, $We_B = 1$. Color depth indicates polymer extension. Note that polymer extension vectors are emphasized and not to scale.

very good. These results generate confidence in the turbulent flow field into which the polymeric phase will be injected.

The influence of the fluid on the polymer extensional vector field is coupled through the transpose of the velocity gradient tensor, κ^* . To generate understanding about the influence of the fluid in various regions of the channel flow, the distributions of velocity gradient components are presented in Fig. 3. The data for these distributions were generated by sampling 10 000 random points within each region, limited to the lower half of the channel flow. Due to the nature of both the mean velocity profile and the presence of coherent turbulent structures at various wall-normal distance regions observed in previous studies into wall-bounded turbulence (Lumley, 1981; Mortimer and Fairweather, 2020; Lee and Moser, 2015; Moser *et al.*, 1999), the analysis shall focus on explaining polymer stretching, and fluid interaction behavior in each of these. The region definitions are presented in Table I.

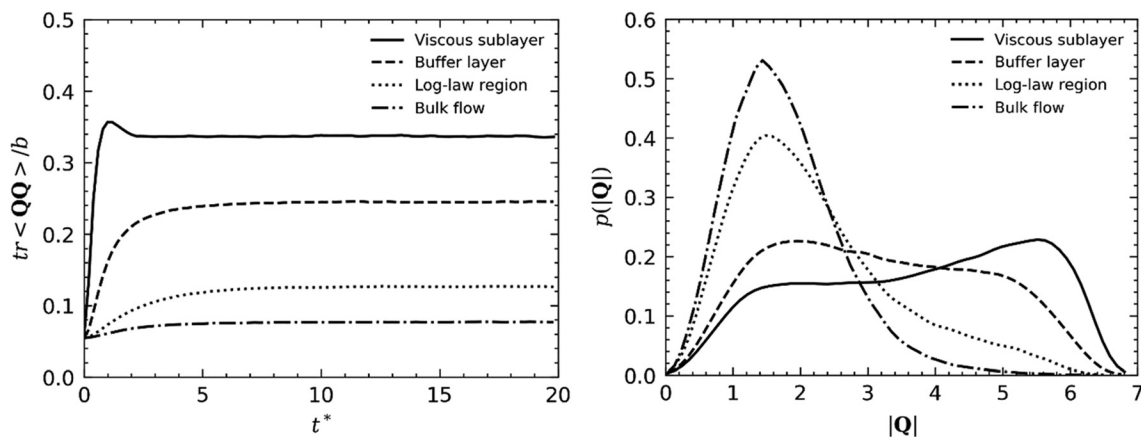


FIG. 5. Temporal evolution of $tr\langle \mathbf{Q}\mathbf{Q} \rangle / b$ (left) and probability distribution of polymer extension $|\mathbf{Q}|$ (right) in turbulent channel flow for $b = 50$, $We_B = 1$. Regional dependence is illustrated.

Starting with the top row in Fig. 3, the results illustrate the variation of streamwise velocity gradients dependent on direction and region. In the streamwise direction, the gradients are relatively low, with the greatest variation and range occurring in the buffer layer. In the viscous sublayer, the streamwise velocity slope is very gentle. As expected, the gradient of streamwise velocity is much greater in the wall region as a function of wall distance, this time strongest in the viscous sublayer, and reducing greatly in the log-law and bulk flow regions. The variation of streamwise velocity gradient with spanwise position is also proportionately high in the buffer layer, as the presence of low-speed streaks causes various steep reductions and increases. In the other regions, this component remains low as the frequency and intensity of turbulence structures are reduced. Considering the wall-normal component in the middle row, the gradient with the streamwise and spanwise directions is very low in all regions but has the largest range within the log-law and bulk flow regions. The gradient of wall-normal velocity with the wall-normal direction is greatest in the buffer layer and least in the regions closest to laminar flow (bulk flow and viscous sublayer), as expected since the fluctuations and vortices are least frequent in these regions. Finally, the lower row indicates the distribution of gradients of spanwise velocity. For the streamwise

component, the distributions in all regions aside from the viscous sublayer are similar but, in all cases, are relatively low. In contrast, the wall-normal component is large, with the largest gradients occurring in the wall region. This is likely due to the presence of counter-rotating vortices in these regions which are orientated in the streamwise direction, ejecting fluid particles initially in a spanwise and then wall-normal motion (Pope, 2000). The turbulent regions also contain the largest range of spanwise component of spanwise velocity gradients, with the presence of vortices in these regions also contributing to this. It is clear from Fig. 3 that the dominant components contributing to polymer stretching in Eq. (7) are $\frac{\partial u_x}{\partial y}$ in the viscous sublayer and buffer layer, $\frac{\partial u_x}{\partial z}$ in the wall region, $\frac{\partial u_y}{\partial y}$ in the buffer and log-law layers, $\frac{\partial u_z}{\partial y}$ in the wall region, and $\frac{\partial u_z}{\partial z}$ in the buffer and log-law layers. The term $\kappa(t) \cdot Q(t)$ in Eq. (7), hence, has dominant contributions to the extension in the streamwise direction, particularly so in the near-wall regions and for polymers with moderate Q_y components, for instance, those orientated perpendicular to the wall. Wall-normal extension will be driven by regions of high $\frac{\partial u_y}{\partial x_i}$ close to the wall, i.e., ejection regions, but these will again favor polymers with already moderate wall-normal orientation or extension. Because of increased streamwise stretching near the wall, the tendency for dominant spanwise

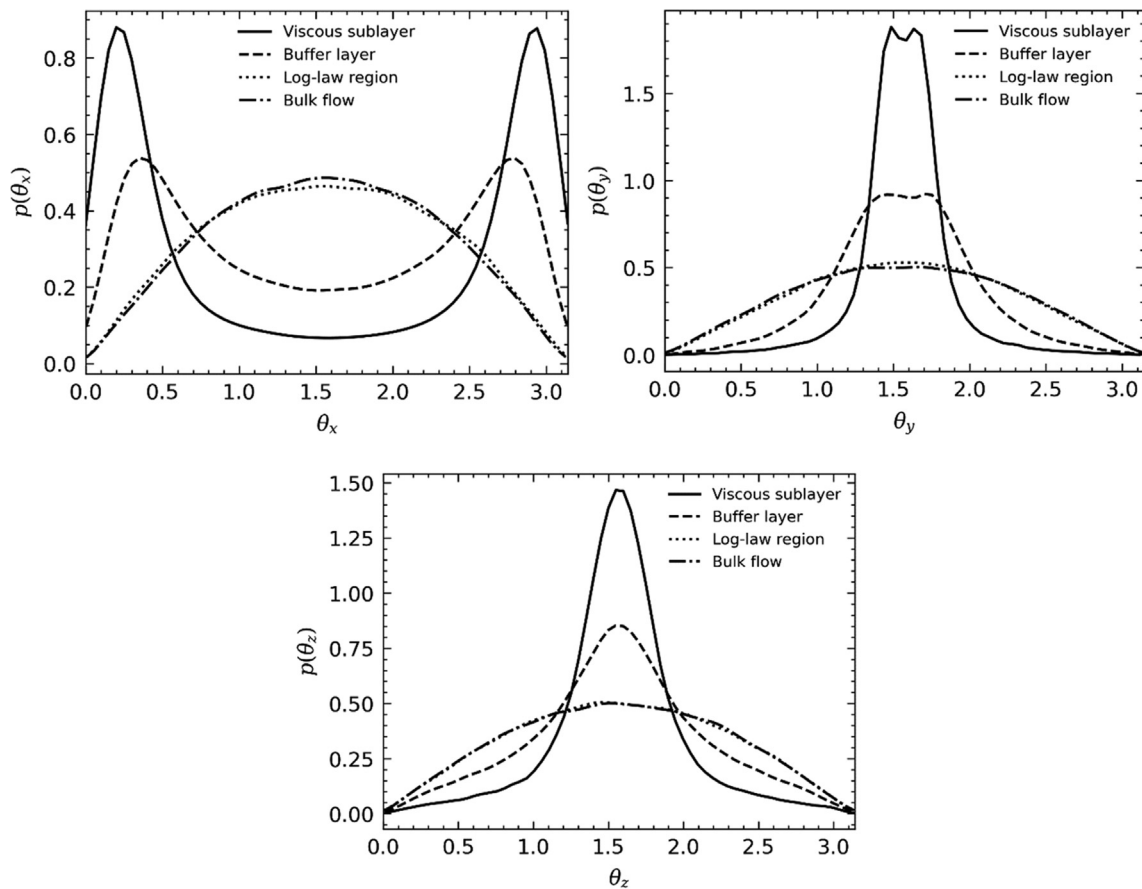


FIG. 6. Probability distribution of angle θ_d made between polymer end-to-end vector Q and streamwise axis (upper-left), wall-normal axis (upper-right), and spanwise axis (lower) for $b = 50$, $We_B = 1$.

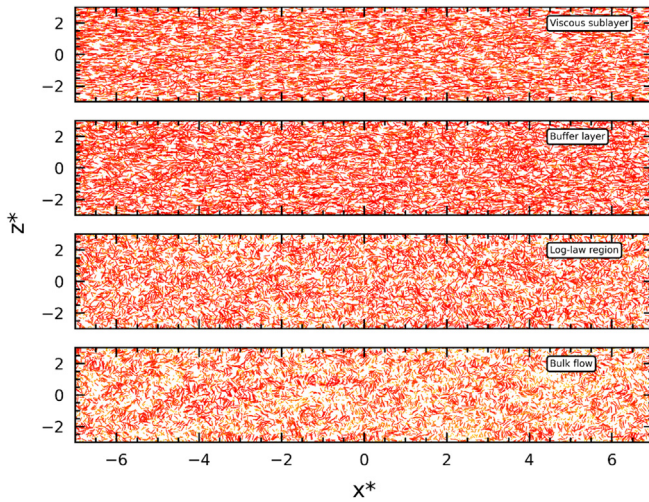


FIG. 7. Instantaneous polymer orientations for $b = 50$, $We_B = 5$. Color depth indicates polymer extension. Note that polymer extension vectors are emphasized and not to scale.

stretching is much less favorable but may happen as a result of streamwise orientated polymers in the bulk flow or the log-law region, where all $\frac{\partial u_i}{\partial x}$ are equally low. That said, stretching to the extent observed in the streamwise direction within the wall region is highly unlikely.

We now consider Newtonian simulations of polymer-laden flows, paying attention predominantly to the polymer configurations in each region of the flow. Three simulations are reported here, with differing polymer timescales $We_B = 1, 5, \text{ and } 10$. The maximum extensibility squared parameter is kept constant at $b = 50$. Since the effect of polymers on the fluid is not considered in this part of the study (effectively $\beta = 1$), 10 000 polymers are injected randomly within the center planes of each of the four fluid regions, on both halves of the channel. For the bulk flow region, polymers are simply injected into the center-plane of the entire channel. Again, the total fluid time studied is $t^* = 20$ in order to ensure statistically stationary

configurations, but within each fluid timestep, the polymers are allowed to evolve for 1000 sub-timesteps to allow time for them to adjust to the local flow variation since the previous step. All results and statistics are reported at the end of $t^* = 20$.

Figure 4 illustrates the polymer orientations and extension for $We = 1$ in each wall-normal region $x^* - z^*$ center plane of the channel flow. In this illustration, polymers are depicted as lines, with the chain colors closer to red indicating longer extensions. Clearly, polymers in the viscous sublayer are mainly orientated in the streamwise direction with various moderate to high extensions. It is notable that the most stretched polymers predominantly align with the streamwise direction. In the buffer layer, we begin to see polymers of moderate extension as well as the appearance of several aligned in the spanwise direction. The presence of “short, upright” chains in this figure may also indicate those orientated in the wall-normal axis direction, but overall an increase in isotropy is observed as the buffer layer is reached. The mean extension is lower than that observed close to the wall, a trend which continues in both the log-law region and the bulk flow region. At $We_B = 1$, there is no obvious alignment with vortical structures close to the wall; however, in both the log-law and the bulk flow regions, there appear to be localized regions of increased extension. The temporal evolution of $tr(\mathbf{Q}\mathbf{Q})/b$ is illustrated in the left plot of Fig. 5, which in all regions demonstrate statistical settling of the conformation tensor by $t^* = 5$. As observed in Fig. 4, the maximum mean extension is found in the viscous sublayer, which reduces as the bulk flow region is approached. The right plot illustrates how the distribution of extensions varies in each wall-normal region. Both the viscous sublayer and the buffer layer contain relatively homogeneous distributions of stretching behavior, whereas the log-law and bulk flow regions tend to favor polymers with low extensions. Since the restoration forces for low We_B polymers are strong, regions of the flow with low fluid-coupling (i.e., regions with low velocity gradient components) do not provide enough energy to maintain even a moderately stretched polymer.

In order to study polymer alignment in each region, the angle the connector vector \mathbf{Q} makes with each axis’ unit vector (i.e., $\theta_i = \cos^{-1} \mathbf{Q} \cdot \hat{e}_i$) was measured and probability distributions are

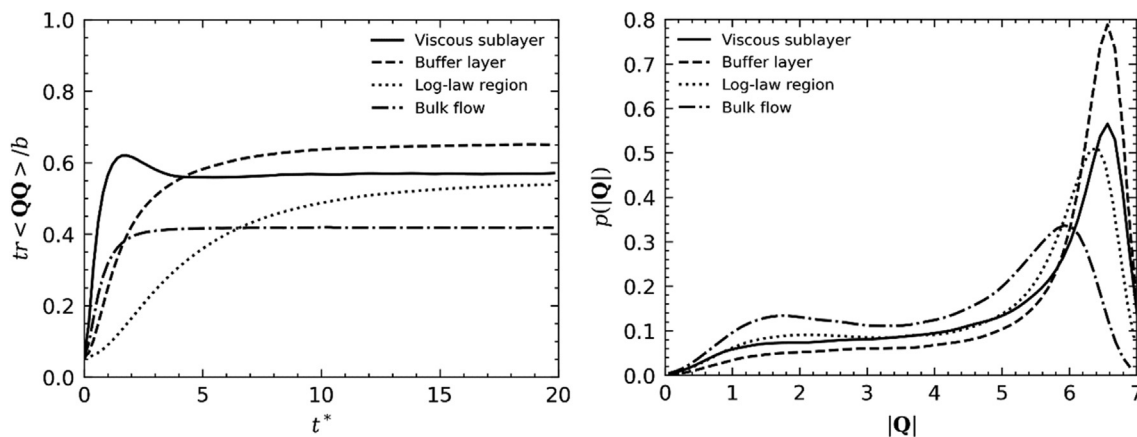


FIG. 8. Temporal evolution of $tr(\mathbf{Q}\mathbf{Q})/b$ (left) and probability distribution of polymer extension $|\mathbf{Q}|$ (right) in turbulent channel flow for $b = 50$, $We_B = 5$. Regional dependence is illustrated.

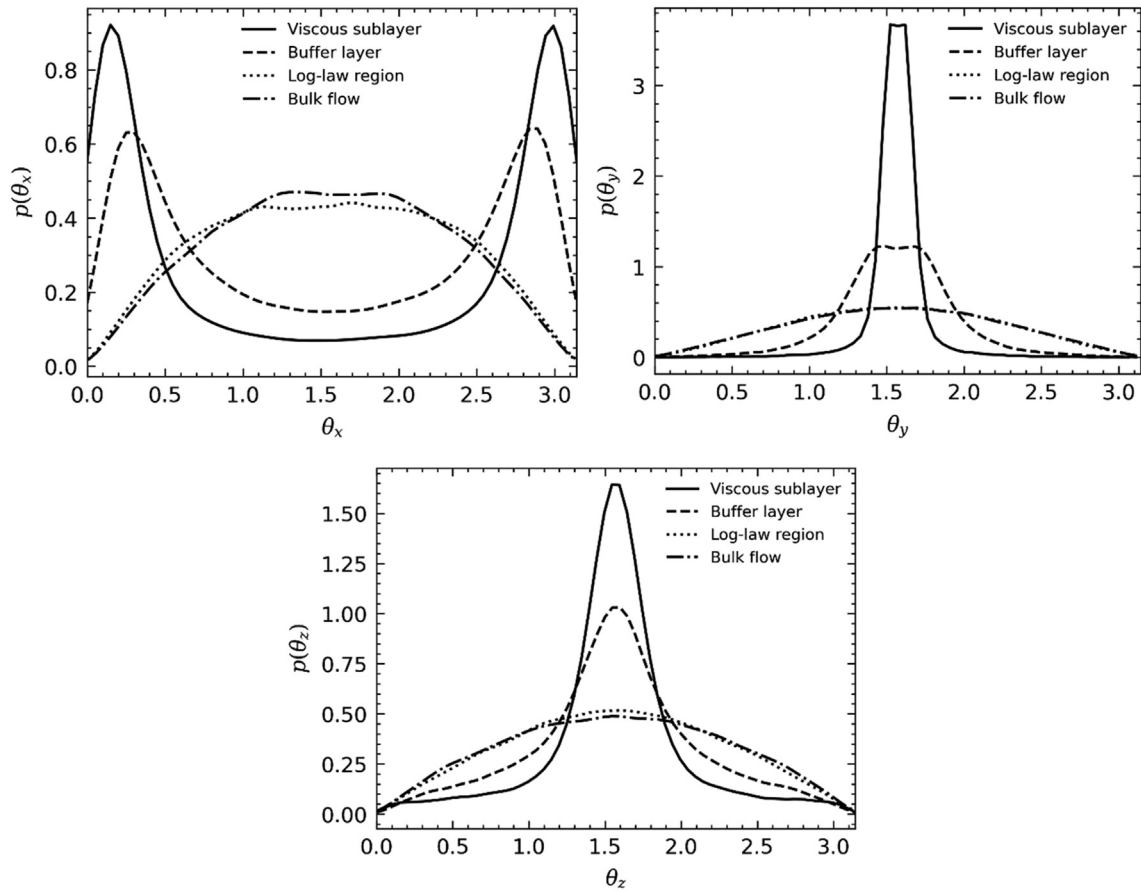


FIG. 9. Probability distribution of angle θ_d made between polymer end-to-end vector \mathbf{Q} and streamwise axis (upper-left), wall-normal axis (upper-right), and spanwise axis (lower) for $b = 50$, $We_B = 5$.

presented in Fig. 6. Note that low ($\theta_i = 0$) and high ($\theta_i = \pi$) angles indicate alignment with axis θ_i . For $We_B = 1$, the top-left plot illustrates obvious alignment with the streamwise axis in the viscous sublayer and buffer layer regions, whereas the most probable alignment in the bulk flow region is to not align with any axis at all, indicating isotropic orientations. The orientation with the streamwise axis in the viscous sublayer and buffer layer is further confirmed in the plots of θ_y and θ_z which show perpendicular orientations to both axes. Again, chains within the viscous sublayer exhibit more dominant streamwise-orientation dynamics. A very interesting behavior is identified in that beyond the buffer layer, polymer orientations are no longer driven by wall distance, despite anisotropic flow conditions and velocity gradient tensor. That said, considering Fig. 3, though the flow conditions are anisotropic, the components of the velocity gradient tensor in these regions tend to be symmetric and also low (when compared to those present in the near-wall layers). The combination of the isotropic Brownian force function with the low fluid coupling term which samples symmetric fluid distributions in these regions likely leads to this eventual isotropy of chain orientation for both regions.

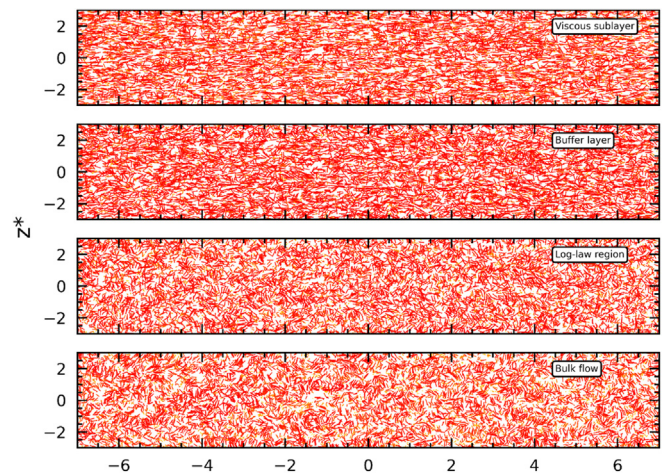


FIG. 10. Instantaneous polymer orientations for $b = 50$, $We_B = 10$. Color depth indicates polymer extension. Note that polymer extension vectors are emphasized and not to scale.

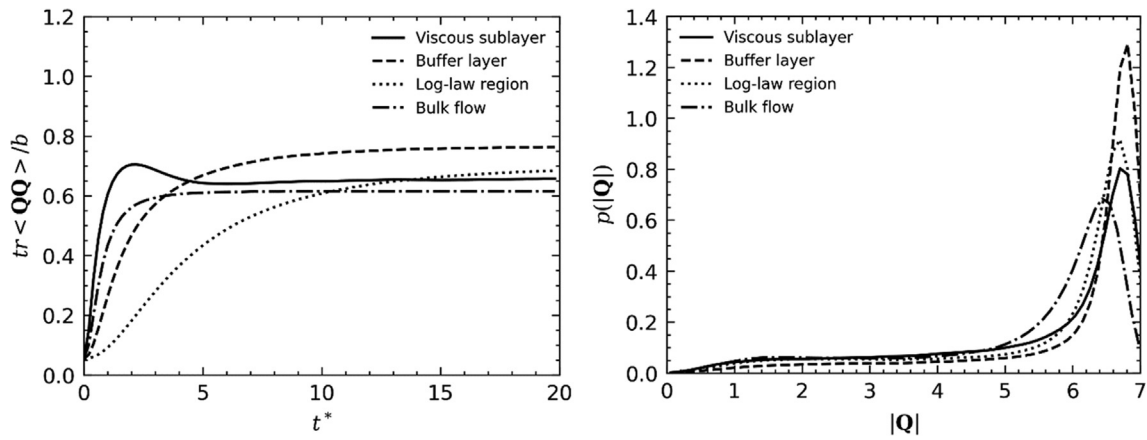


FIG. 11. Temporal evolution of $tr\langle QQ \rangle / b$ (left) and probability distribution of polymer extension $|Q|$ (right) in turbulent channel flow for $b = 50$, $We_B = 10$. Regional dependence is illustrated.

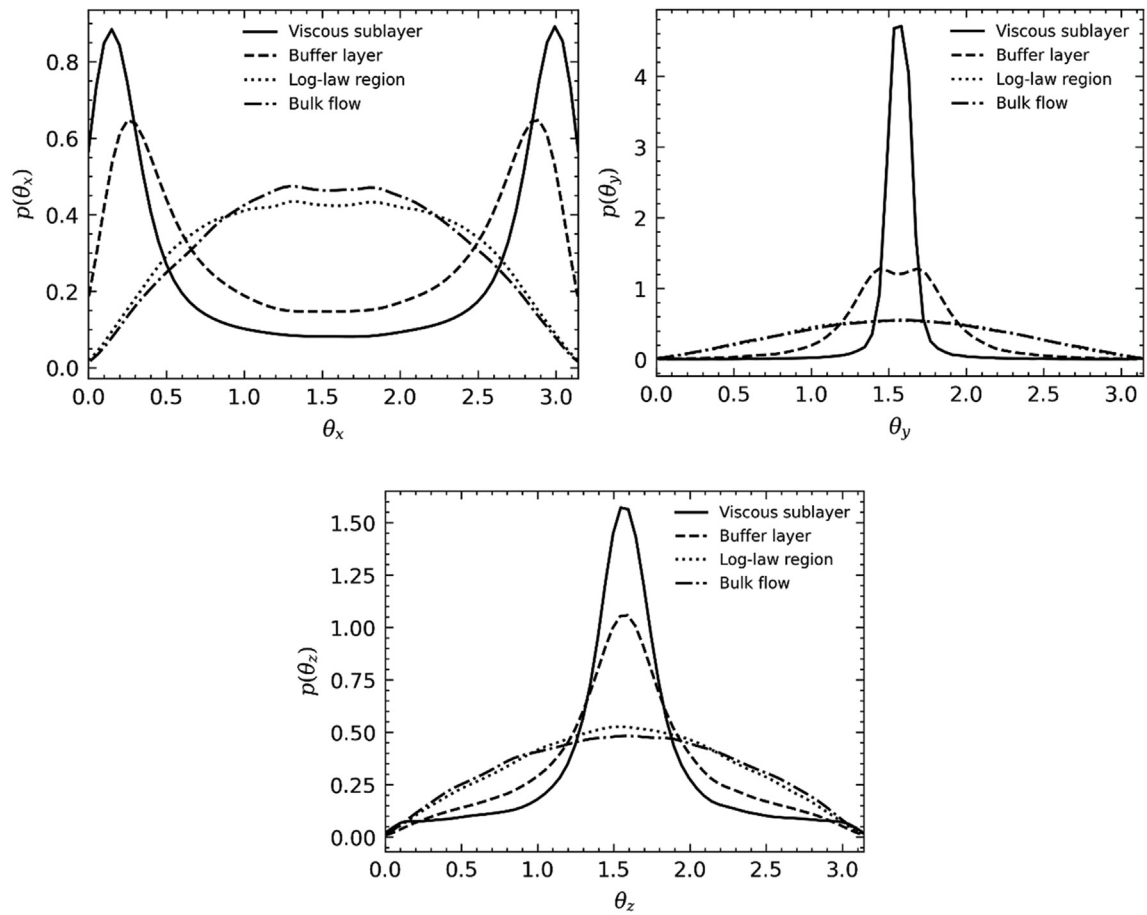


FIG. 12. Probability distribution of angle θ_d made between polymer end-to-end vector Q and streamwise axis (upper-left), wall-normal axis (upper-right), and spanwise axis (lower) for $b = 50$, $We_B = 10$.

For the $We_B = 5$ simulations, it is clear from Fig. 7 that this system exhibits an overall increase in stretching behavior when compared to the $We_B = 1$ case. Here, the largest extensions still occur in the viscous sublayer and the buffer layer, whereas those closer to the bulk flow region are more relaxed. In terms of polymer orientations, the log-law and bulk flow regions also look qualitatively similar, with a slight increase in stretching behavior in the log-law region. In both cases, the polymers appear to trace some of the flow structures, where local orientations appear correlated. The chains in the two regions closest to the wall are predominantly orientated in the streamwise direction. The left plot in Fig. 8 indicates that the largest mean extension was this time found within the buffer region, indicating a transition point between $We_B = 1-10$ where the mechanisms leading to the longest extensions become more dominant beyond the viscous sublayer. Comparing against the instantaneous plot in Fig. 7, this seems to be the case. It is also of value to note that the polymers within the log-law region take up to $t^* = 20$ for the conformation tensor to reach an approximate steady state.

We believe the explanation is as follows. There are two fluid-coupling mechanisms at play here through which a statistically stationary state is eventually reached. These are chain extension and

reorientation. For the low Weissenberg number, the extension mechanism is weak, hence only the reorientation mechanism occurs. As the Weissenberg number is increased, the log-law region now has both extension (see Fig. 8) and reorientation (see Fig. 9) as opposed to the buffer and viscous sublayer regions which are primarily driven by streamwise extension dynamics and the bulk flow region which is primarily driven by reorientation dynamics with low extension. The combination of these two mechanisms likely leads to a longer statistical settling timescale. The right plot in Fig. 8 again illustrates the shift in the peak of the extension probability distribution within the buffer layer to be greater than that of the viscous sublayer. We also observe that in all regions, longer extensions are preferred over shorter ones. This is expected as the timescale parameter, We_B , determines the dominance of the terms of the force balance in Eq. (7). With an increase in We_B , the hydrodynamic term becomes larger in comparison to the nonlinear restoring spring force term as well as the stochastic Brownian term. In effect, the resistance to stretching is reduced. Figure 9 illustrates the orientation of the polymers within each wall-normal region. Despite the largest stretching taking place within the buffer layer, the polymers orientate themselves the most with the streamwise axis in the viscous sublayer. Again, orientations within the

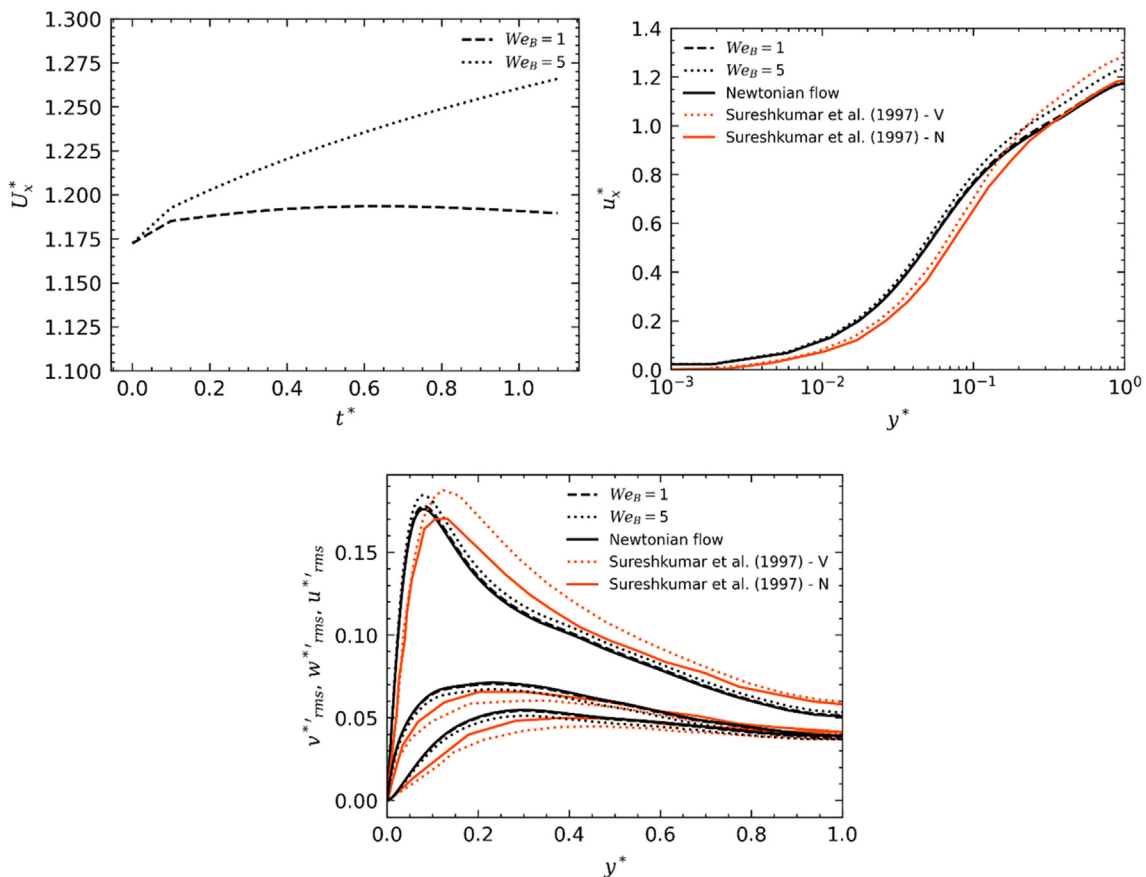


FIG. 13. Temporal evolution of centerline streamwise velocity U_x^* (upper left), mean streamwise velocity (upper right), and root mean square of velocity fluctuations (lower) sampled at $t^* = 10$ and for $\beta = 0.9$. Comparison between We_B and Newtonian flow is illustrated. A comparison against the observed effects of the Newtonian (N) and drag reduced viscoelastic (V) statistics of Sureshkumar et al. (1997) at $Re_\tau = 125$ is also demonstrated.

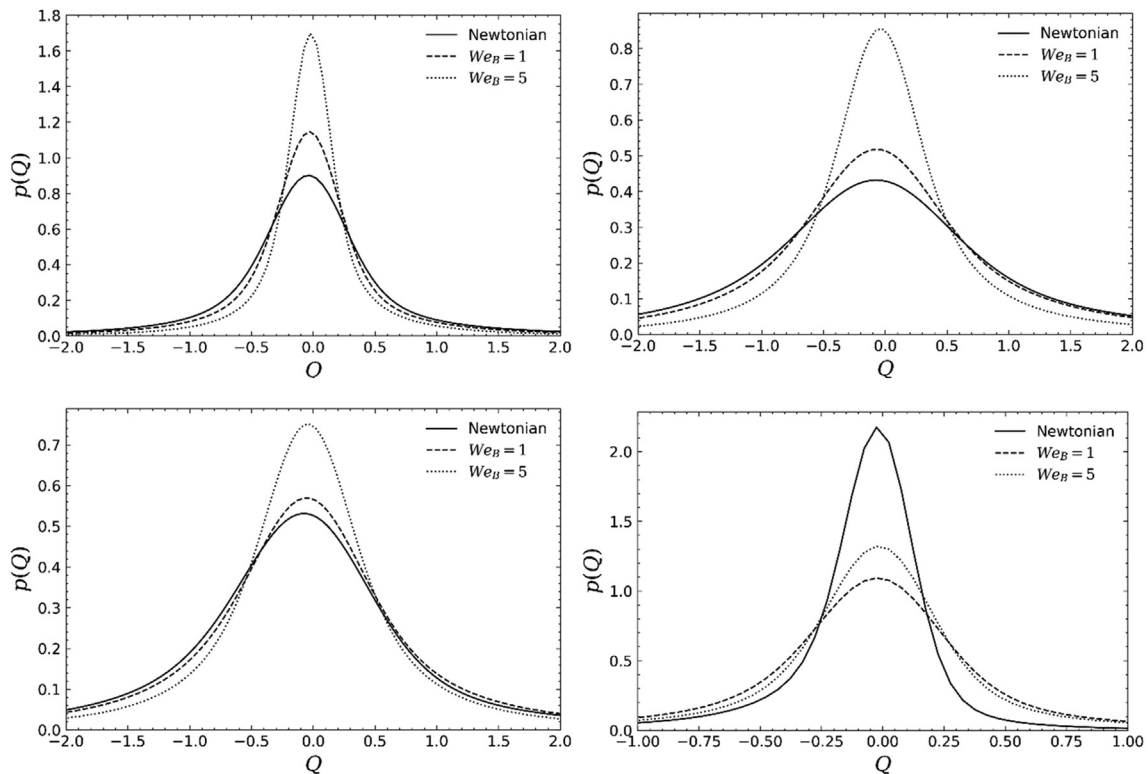


FIG. 14. Comparison of velocity gradient tensor invariant, Q , sampled in fluid wall-normal regions: bulk flow (upper-left), log-law region (upper-right), buffer layer (lower-left), and viscous sublayer (lower-right). Effect of bulk Weissenberg number, We_B , is indicated.

log-law and bulk flow regions are relatively randomly distributed. It is theorized here that polymers within the buffer layer undergo additional stretching in the wall-normal and spanwise directions through interaction with the $\frac{du_y}{dy}$ and $\frac{du_z}{dz}$ components of the velocity gradient tensor, both of which are strongest in the buffer layer (see Fig. 3) and contribute to stretching perpendicular to the streamwise direction. However, considering the top-right and lower plots of Fig. 9, the mechanism drives the state more toward isotropy, rather than toward orientating toward an alternative axis, since the distributions only widen, with no indication of a peak at $\theta_i = 0$ or $\theta_i = \pi$.

Finally, we consider the dynamics for $We_B = 10$. Figure 10 indicates similar qualitative characteristics to those corresponding to $We_B = 5$, with relatively streamwise-orientated stretching occurring in the near-wall region and local coherent orientations occurring in the log-law and bulk flow regions. The chain extension lengths in all regions are saturated by almost fully extended polymer configurations, indicating that the dominant mechanism driving extension is occurring in all regions. Figure 11 (left) further reorders the regions of highest mean extension, with the buffer layer remaining highest, followed by the log-law region, the viscous sublayer, and the bulk flow region. Again, the log-law region takes the longest for the configuration of polymer extensions to reach an approximately statistically stationary state. Considering the right plot in Fig. 11, all regions now favor high-

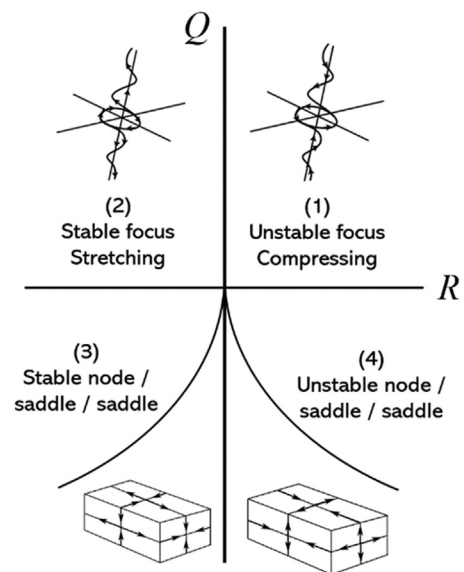


FIG. 15. Q and R tensor invariants for incompressible flow turbulent structure topology classification. Solid curved lines represent $D = \left(\frac{27}{4}\right)R^2 + Q^3 = 0$.

extensional states, with low ($|Q| < 5$) extensions highly improbably. In fact, a vast proportion of polymers possess extensions close to their maximum extensibility $L = \sqrt{50}$. As with the $We_B = 5$ case, polymers are most orientated in the streamwise direction in the viscous sublayer and buffer layer; however, this time, we observe a slight widening of the θ_x distribution in the log-law region, indicating a tendency for anisotropy when compared to the bulk flow orientations. Beyond $We_B = 1$, the orientations, therefore, seem fairly independent of the relaxation timescale of the polymer. This is reflected in Fig. 12, which illustrates the orientation of polymers in the flow with $We_B = 10$. Comparing with Fig. 9, the distributions are very similar, indicating that the mechanisms which orientate the chains become Weissenberg number-independent. This is likely due to the polymers behaving more rigidly, sampling only extensions close to their maximum extensibility. Their rotational behavior is then similar to those with the same high extensions but at $We_B = 5$.

B. Viscoelastic dynamics in polymer-laden turbulent channel flow at $Re_\tau=180$

In this section, we consider the effect of We_B on the changes in rheological properties caused by viscoelastic contributions to the stress tensor from polymer additives. Moving forward, instead of $\beta = 1$ (i.e., Newtonian flow dynamics), we reduce this parameter to $\beta = 0.9$, in

line with previous studies of this nature. Furthermore, due to the similarities exhibited in Sec. III A surrounding extensional behavior for $We_B = 5$ and $We_B = 10$ in the systems with no viscoelastic mechanisms considered, we choose to consider the effects of only the $We_B = 1$ and $We_B = 5$ systems. In each simulation, 100 polymers per GLL cell were injected. The fluid timestep in the viscoelastic case remains constant at $\delta t^* = 1 \times 10^{-3}$, chosen to ensure stability when calculating the additional polymer stress tensor field. We found that larger timesteps, such as those used in the Newtonian case, would lead to increased changes in the calculated fluid stress tensor, which caused divergence issues. At each timestep, each unique GLL cell performs local Brownian dynamic simulations, ensuring that the calculated mean end-to-end extension vector is smooth with time. Once a cell had a statistically stationary configuration tensor, Eqs. (5) and (6) were used to calculate the local additional stress tensor, which would then be used for the next fluid simulation step.

Statistics were sampled after the flow had responded and reached a statistically steady state after the injection of polymers. From Fig. 13(upper-left), in both cases, we observe a steady increase with time in the centerline streamwise velocity, which is stronger for the $We_B = 5$ case. In both cases, $t^* = 1$ is sufficient time for this to take place. In the upper-right plot of Fig. 13, the mean streamwise velocity increases beyond the viscous sublayer region (which has widened), demonstrating the expected drag-reduction, as observed in many

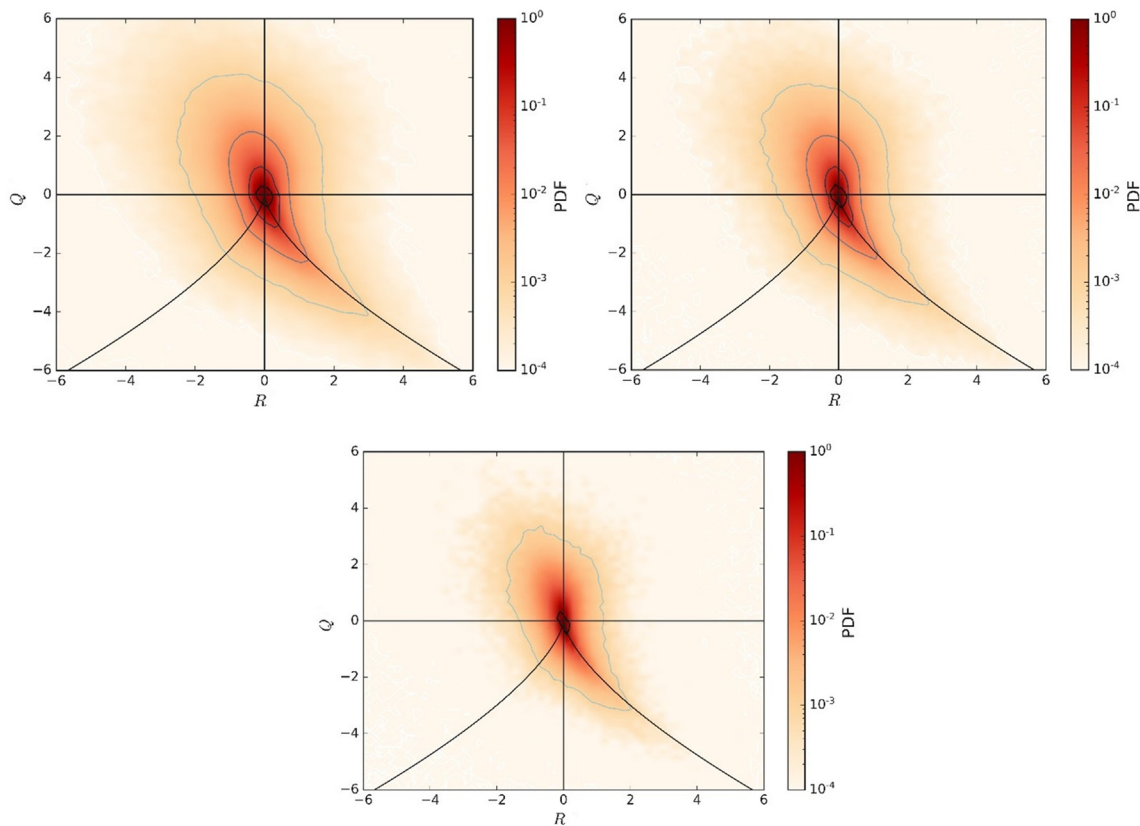


FIG. 16. PDFs of invariants of the velocity gradient tensor, Q and R , sampled at fluid nodes in the bulk flow region. Upper left: Newtonian flow, upper right: $We_B = 1$, and lower: $We_B = 5$.

experimental studies (Pinho and Whitelaw, 1990; Wei and Willmarth, 1992). Comparison is made in Fig. 13 with the results of Sureshkumar *et al.* (1997), who also considered simulation of drag reduction at $\beta = 0.9$, albeit at $Re_\tau = 125$. Their Newtonian and viscoelastic results for $We_\tau = 50$ (equivalent to $We_B = 5.88$) are displayed in the plots to illustrate the qualitative drag reduction effects. We observe the same trend, and in the case of Sureshkumar *et al.* (1997), the magnitude of the drag reduction is increased due to a slightly increased Weissenberg number. Furthermore, for their $We_\tau = 12.5$ (equivalent to $We_B = 1.47$) simulation, they obtained a 2.5% increase in the mean flow velocity. This is in line with our findings of a 1.7% since our Weissenberg number was slightly lower. The authors began to see obvious drag reduction at $We_\tau = 25$ ($We_B = 2.94$) which is in agreement with our findings, as by $We_B = 5$, the drag reduction is obvious.

Finally, their predictions for the components of the rms velocity fluctuations are also in qualitative agreement with the present work. The turbulence levels, indicated by the root mean square of the velocity fluctuations in the lower plot of Fig. 13, are enhanced throughout the bulk flow region in the streamwise direction and reduced in the wall-normal and spanwise directions. This is indicative of the suppression of energy redistribution between the streamwise to the wall-normal and spanwise directions and has been observed in previous studies (Li *et al.*, 2015), with increasing We_B leading to these effects

becoming stronger. To further investigate the influence of the polymeric phase on the flow, the effect of Weissenberg number on the properties of coherent turbulent structures was also considered. Figure 14 illustrates the modification to the velocity gradient invariant, Q , often used to characterize vortex regions in turbulent flows. There exist multiple methods used in the literature to classify both the structure and strength of coherent turbulent flow structures. A commonly employed technique is that, based on the velocity gradient tensor, $D_{ij} = \frac{\partial u_i}{\partial x_j}$. This tensor is often decomposed into its symmetric (rate-of-strain) and antisymmetric (vorticity) tensor components such that $D_{ij} = S_{ij} + \Omega_{ij}$, with $S_{ij} = \frac{1}{2} \left(\frac{\partial u_i}{\partial x_j} + \frac{\partial u_j}{\partial x_i} \right)$ and $\Omega_{ij} = \frac{1}{2} \left(\frac{\partial u_i}{\partial x_j} - \frac{\partial u_j}{\partial x_i} \right)$. The Q -criterion refers to the condition applied to the second invariant, Q , of the velocity gradient tensor, where $Q = \frac{1}{2} (\|\Omega\|^2 - \|S\|^2)$. Note that in the present study, Q is non-dimensionalized by bulk quantities (U_B^2/δ^2). The vortex condition is such that if $Q > 0$ (i.e., the vorticity is greater than the shear strain rate) is satisfied in a particular fluid cell, then the fluid element contains part of a vortex. In the cases considered here, the range of Q values sampled in each flow region is reduced with the presence of the polymeric phase, and with increasing We_B . The most dominant structures within the buffer layer are quasi-streamwise hairpin vortices which convect slow-moving regions of fluid to the bulk flow region, whereas faster fluid streamlines are convected

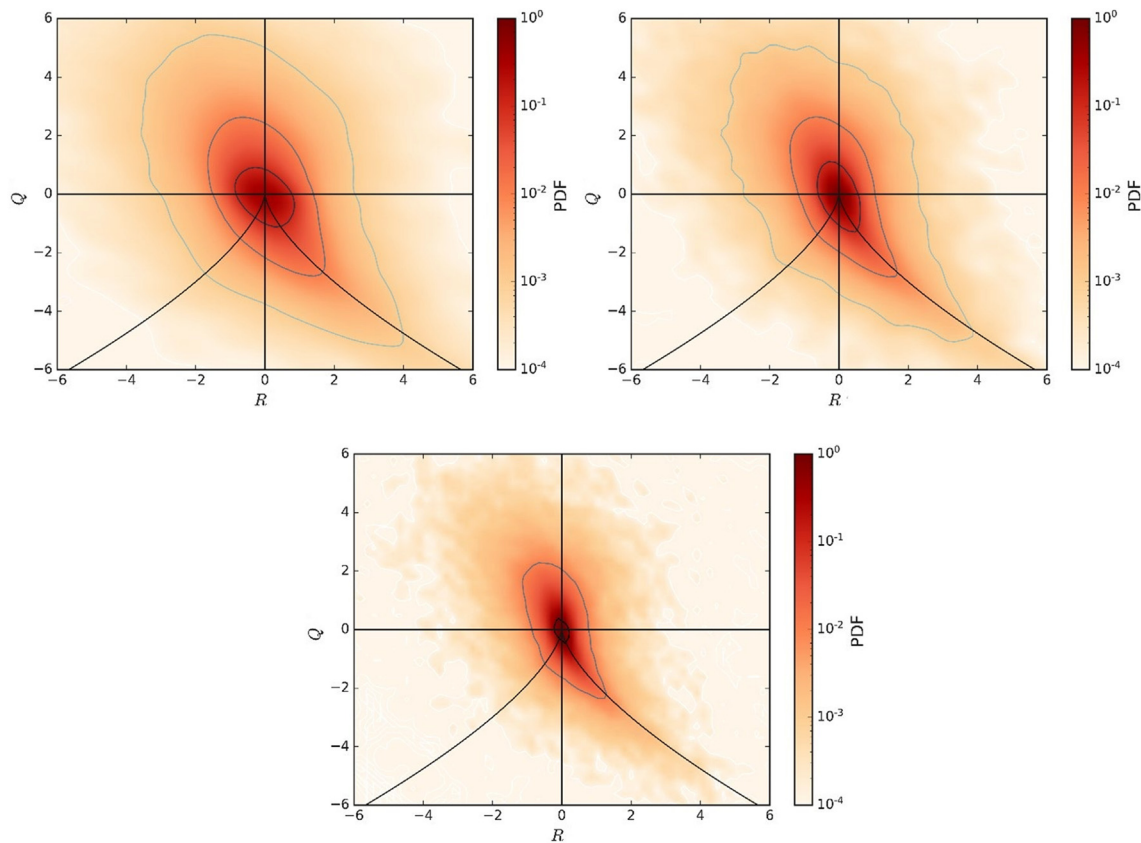


FIG. 17. PDFs of invariants of the velocity gradient tensor, Q and R , sampled at fluid nodes in the log-law region. Upper left: Newtonian flow, upper right: $We_B = 1$, and lower: $We_B = 5$.

toward the buffer layer. A reduction in Q within these regions implies that the turbulent structures are less frequent or that those which still survive are dampened. Most interestingly, regions of increased magnitude of Q are actually increased in the viscous sublayer, with the effect lessened by an increased We_B . It is difficult from these results alone to discern the full effect on the structure of turbulence. To investigate further, we adopt the classification scheme of Blackburn *et al.* (1996). Under this classification, each fluid field point is categorized using one of four turbulent structure topology definitions. These are unstable focus/compressing, stable focus/stretching, stable node/saddle/saddle, and unstable node/saddle/saddle, as illustrated in Fig. 15. Here, R is the third invariant of the velocity deviatoric tensor, equivalent to the negative product of all three of its eigenvalues and is normalized using bulk quantities, U_B^3/δ^3 .

The effect of We_B on the Q - R phase portrait for fluid points sampled in the bulk flow region is presented in Fig. 16. Comparing to the Newtonian flow, the vortical-region effect due to the presence of polymers is clear, with the distribution narrowing in both directions for increasing Weissenberg number. The characteristic shape of the phase portrait remains consistent, indicating a general reduction in vortex strength while retaining the same structure. Since polymer chains tend to be the least stretched in the bulk flow region, the energy removed from the vortices causes a slight dampening effect but isotropically as

indicated by the distributions of chain orientation. Due to this, the topology of the turbulent structures is minimally affected. Moving on to the log-law region in Fig. 17, we begin to observe a narrowing of the range of R as the Weissenberg number increases, leading to stronger foci-type regions. There is also a slight stretching in Q for regions of low R which is characteristic of a flow structure becoming more two-dimensional. The effect is more pronounced for the high We_B simulation, where most of the distribution is concentrated at low Q and R .

Similar observations are made in the buffer layer for Fig. 18, with the narrowing in R still persisting. This time, however, distributions for $We_B = 1$ and $We_B = 5$ are similar in shape, indicating that the modification to the topology of the coherent turbulent structures in this region may be saturated beyond a certain Weissenberg number. In both of these cases, the buffer layer contains mostly fully stretched polymers, which may explain the similarities between these two systems within this region.

Finally, the phase portrait for the viscous sublayer, shown in Fig. 19, illustrates the same narrowing in R but a much more enhanced stretching of Q . The presence of polymers in the viscous sublayer increases the frequency of vortical regions with increased Q , particularly for those regions with low R . Again, this is indicative of the flow becoming more two-dimensional close to the wall. This enhancement of Q , particularly for positive Q , is indicative of an increase in both

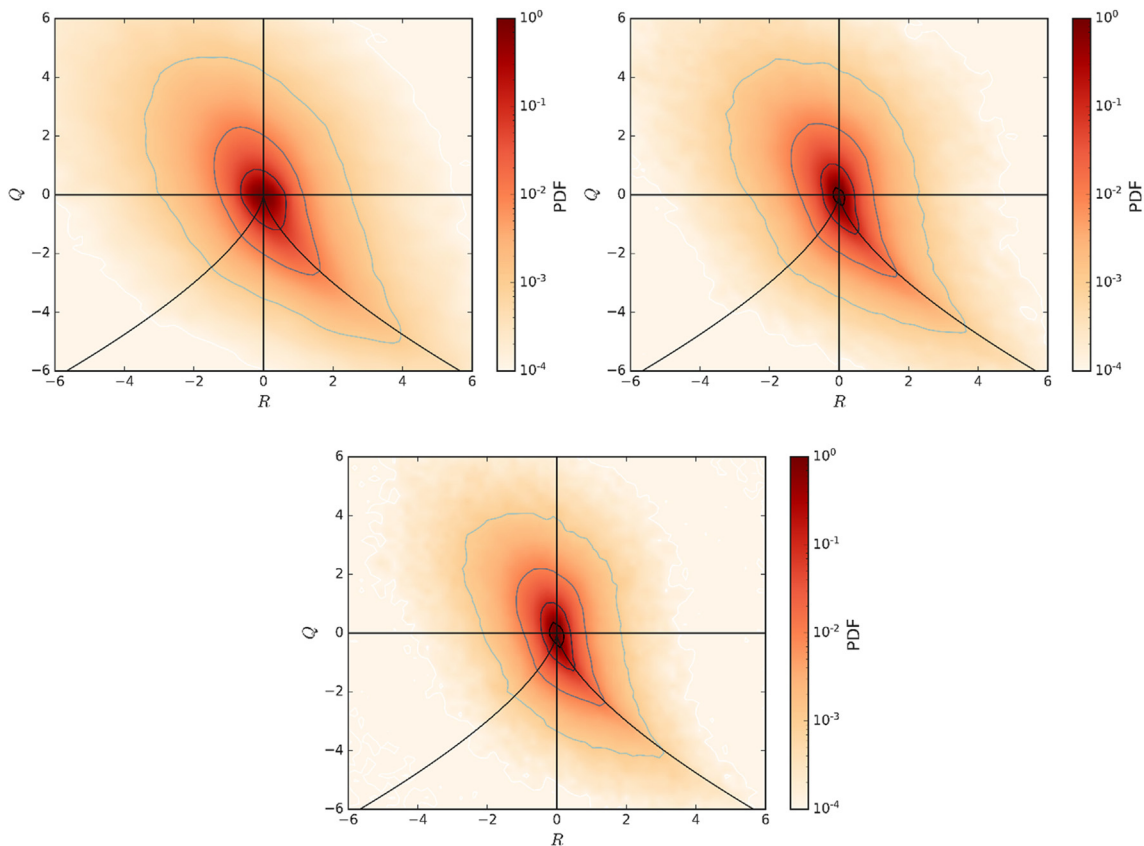


FIG. 18. PDFs of invariants of the velocity gradient tensor, Q and R , sampled at fluid nodes in the buffer region. Upper left: Newtonian flow, upper right: $We_B = 1$, and lower: $We_B = 5$.

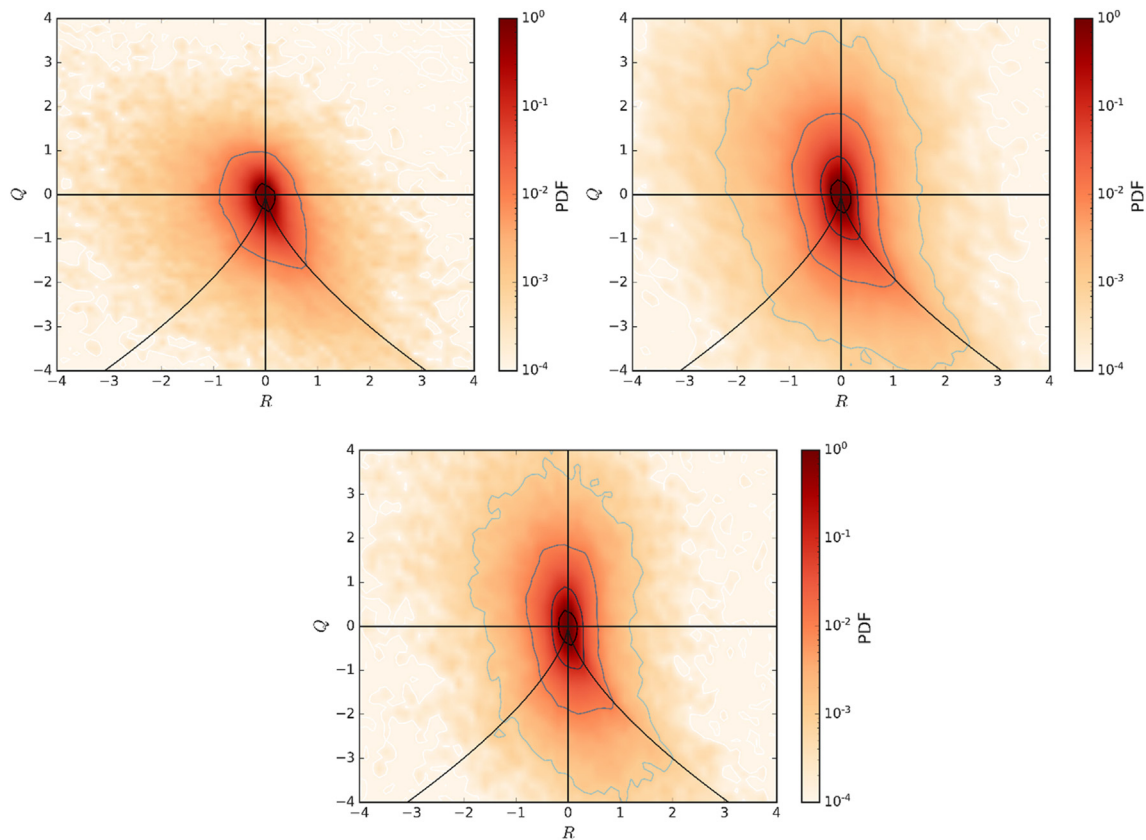


FIG. 19. PDFs of invariants of the velocity gradient tensor, Q and R , sampled at fluid nodes in the viscous sublayer. Upper left: Newtonian flow, upper right: $We_B = 1$, and lower: $We_B = 5$.

compressing and stretching foci. Given that most of the polymers in this region tend to be fully extended, there is likely an abundance of elastic energy which may be transferred to the local vortices as the polymers contract within this region, which may explain the enhancement of the strength of these structures.

IV. CONCLUSIONS

Polymer extension and viscoelastic coupling have been studied using simulations of a drag-reduced turbulent channel flow at $Re_\tau = 180$. A multiscale hybrid approach is adopted, whereby direct numerical simulation is used to predict the continuous phase while Brownian dynamics simulations and the FENE dumbbell approach are carried out to model the trajectories of polymer extension vectors. Parallel computations have been performed to achieve improved computation timeframes for a highly resolved flow. Strong agreement was observed between the polymeric configurations observed in the simulations and theoretical predictions in equilibrium conditions.

To determine the influence of the continuous phase on the polymer extensional vectors, distributions of velocity gradient tensor components are analyzed throughout the channel flow wall-normal regions. These are key to understanding polymer extension and fluid coupling since they directly affect the time evolution of the mean conformation tensor. We observed that, in the streamwise direction,

gradients of velocity were low, with the strongest gradients occurring in the buffer layer. The presence of turbulent structures in this region, such as low-speed streaks, augments polymer–fluid interaction leading to more significant extension. The dominant components contributing to polymer stretching were determined to be $\frac{\partial u_x}{\partial y}$ in the viscous sublayer and buffer layer, $\frac{\partial u_x}{\partial z}$ in the wall region, $\frac{\partial u_x}{\partial y}$ in the buffer and log-law layers, $\frac{\partial u_x}{\partial y}$ in the wall region, and $\frac{\partial u_x}{\partial z}$ in the buffer and log-law layers. Most of these terms contribute to the streamwise extension, causing the polymer chains to orientate themselves in the flow direction, using the energy of the near-wall vortices to extend. We also note that moderate wall-normal extensions close to the wall will further augment the streamwise stretching, causing a curling effect, which we demonstrate occurring in the log-law and bulk flow regions.

Further effects are observed in instantaneous snapshots of polymer extension throughout wall-normal slices of the turbulent channel flow, with the effects of the bulk Weissenberg number demonstrating that increased We_B leads to larger extensions and more streamwise orientated conformities close to the wall. In the bulk flow and log-law regions, the polymers tend to trace turbulent structures in the fluid. The time required to reach a statistically stationary state for the conformation tensor is measured, of use in determining the time required for polymeric simulations during a single fluid timestep to achieve accuracy and precision. In most cases, $t^* = 10$ was sufficient, with the

log-law and buffer layers taking longer for high We_B . For these cases, most polymers approached their maximum extensibility, whereas the distributions exhibited a good proportion of unextended polymers for the lower We_B . Chain orientation angles are also measured, with We_B demonstrating little influence on the isotropic distributions in the log-law and bulk flow regions.

Polymer–fluid coupling is implemented through a polymer contribution to the viscoelastic stress tensor, calculated using the mean conformation tensor at each GLL cell in the domain. The effect of the Weissenberg number on turbulent drag reduction effects has been discussed, with high polymer relaxation times leading to more impactful reductions. The streamwise turbulence intensities are augmented by the presence of polymers, while the other two components are reduced. Finally, the velocity gradient tensor invariants are calculated for the drag-reduced flows, with polymers having a significant impact on the Q–R phase diagrams. In all regions, aside from the viscous sublayer, the strength of the vortical structures is reduced, with the presence of polymers tending to cause the distribution of R to narrow. Interestingly, the distribution of Q is widened in the viscous sublayer, perhaps due to fully extended streamwise orientated chains in this region contracting and introducing energy to the local vortex structures.

Often, particularly in industrial applications, further consideration of a transported particulate phase is required. In this study, we have demonstrated that polymers can modify the turbulent structures within wall-bounded flows. Previous studies (Mortimer and Fairweather, 2020; Dizaji and Marshall, 2017; Eaton, 2009), however, indicate that capturing particle–turbulence interaction is pivotal to the accurate prediction of particle trajectories, which may differ greatly upon the addition of polymers. Therefore, systems containing both phases should be studied. The mechanisms by which both particles and polymers interact under the influence of various flows are also of great interest to processes such as flocculation and separation, and so, future work will consider the micro-scale interactions of polymers and particles to generate more useful insight into the micro-scale interaction events. Finally, a comparison of the present findings with those predicted when using other constitutive relationships (Giesekus, Oldroyd-B) for the viscous stress tensor should be considered and compared to experimental validation data, when available, in order to determine appropriateness in various cases.

ACKNOWLEDGMENTS

The authors are grateful for funding from the UK Engineering and Physical Sciences Research Council through the TRANSCEND (Transformative Science and Engineering for Nuclear Decommissioning) project (No. EP/S01019X/1).

AUTHOR DECLARATIONS

Conflict of Interest

The authors have no conflicts to disclose.

Author Contributions

Lee Mortimer: Conceptualization (equal), Data curation (equal), Formal analysis (equal), Investigation (equal), Methodology (equal), Project administration (equal), Software (equal), Validation (equal),

Visualization (equal), Writing – original draft (equal), and Writing – review and editing (equal). **Michael Fairweather:** Funding acquisition (equal), Supervision (equal), Writing – original draft (equal), and Writing – review and editing (equal).

DATA AVAILABILITY

The data that support the findings of this study are available from the corresponding author upon reasonable request.

REFERENCES

- Azaiez, J., and Homsy, G. M., “Linear stability of free shear flow of viscoelastic liquids,” *J. Fluid Mech.* **268**, 37–69 (1994a).
- Azaiez, J., and Homsy, G. M., “Numerical simulation of non-Newtonian free shear flows at high Reynolds numbers,” *J. Non-Newtonian Fluid Mech.* **52**, 333–374 (1994b).
- Benzi, R., Ching, E. S., Horesh, N., and Procaccia, I., “Theory of concentration dependence in drag reduction by polymers and of the maximum drag reduction asymptote,” *Phys. Rev. Lett.* **92**, 078302 (2004).
- Berman, N. S., “Drag reduction by polymers,” *Annu. Rev. Fluid Mech.* **10**, 47–64 (1978).
- Bird, R. B., Curtiss, C. F., Armstrong, R. C., and Hassager, O., *Dynamics of Polymeric Liquids*, Vol. 2: Kinetic Theory (Wiley, 1987).
- Blackburn, H. M., Mansour, N. N., and Cantwell, B. J., “Topology of fine-scale motions in turbulent channel flow,” *J. Fluid Mech.* **310**, 269–292 (1996).
- Blackwelder, R., and Kaplan, R., “On the wall structure of the turbulent boundary layer,” *J. Fluid Mech.* **76**, 89–112 (1976).
- Choi, H., Moin, P., and Kim, J., “Active turbulence control for drag reduction in wall-bounded flows,” *J. Fluid Mech.* **262**, 75–110 (1994).
- Dizaji, F. F., and Marshall, J. S., “On the significance of two-way coupling in simulation of turbulent particle agglomeration,” *Powder Technol.* **318**, 83–94 (2017).
- Dubief, Y., Terrapon, V. E., and Soria, J., “On the mechanism of elasto-inertial turbulence,” *Phys. Fluids* **25**, 110817 (2013).
- Eaton, J. K., “Two-way coupled turbulence simulations of gas-particle flows using point-particle tracking,” *Int. J. Multiphase Flow* **35**, 792–800 (2009).
- Edomwonyi-Otu, L. C., and Adelakun, D. O., “Effect of heavy molecular weight polymer on quality of drinking water,” *Mater. Today Commun.* **15**, 337–343 (2018).
- Figueredo, R., and Sabadini, E., “Firefighting foam stability: The effect of the drag reducer poly (ethylene) oxide,” *Colloids Surf., A* **215**, 77–86 (2003).
- Fischer, P. F., Lottes, J. W., and Kerkemeier, S. G., see <http://nek5000.mcs.anl.gov> for “Nek5000, 2008.”
- Fouxon, A., and Lebedev, V., “Spectra of turbulence in dilute polymer solutions,” *Phys. Fluids* **15**, 2060–2072 (2003).
- Garg, P., Chaudhary, I., Khalid, M., Shankar, V., and Subramanian, G., “Viscoelastic pipe flow is linearly unstable,” *Phys. Rev. Lett.* **121**, 024502 (2018).
- Gordon, R., and Balakrishnan, C., “Vortex inhibition: A new viscoelastic effect with importance in drag reduction and polymer characterization,” *J. Appl. Polym. Sci.* **16**, 1629–1639 (1972).
- Gu, Y., Yu, S., Mou, J., Wu, D., and Zheng, S., “Research progress on the collaborative drag reduction effect of polymers and surfactants,” *Materials* **13**, 444 (2020).
- Gupta, V., Sureshkumar, R., and Khomami, B., “Polymer chain dynamics in Newtonian and viscoelastic turbulent channel flows,” *Phys. Fluids* **16**, 1546–1566 (2004).
- Herrchen, M., and Öttinger, H. C., “A detailed comparison of various fene dumbbell models,” *J. Non-Newtonian Fluid Mech.* **68**, 17–42 (1997).
- Hetsroni, G., Zakin, J. L., and Mosyak, A., “Low-speed streaks in drag-reduced turbulent flow,” *Phys. Fluids* **9**, 2397–2404 (1997).
- Ilg, P., De Angelis, E., Karlin, I., Casciola, C., and Succi, S., “Polymer dynamics in wall turbulent flow,” *Europhys. Lett.* **58**, 616 (2002).
- Kumar, S., and Homsy, G. M., “Direct numerical simulation of hydrodynamic instabilities in two- and three-dimensional viscoelastic free shear layers,” *J. Non-Newtonian Fluid Mech.* **83**, 249–276 (1999).

- Lee, M., and Moser, R. D., "Direct numerical simulation of turbulent channel flow up to $Re_\tau = 590$," *J. Fluid Mech.* **774**, 395–415 (2015).
- Li, C. F., Sureshkumar, R., and Khomami, B., "Simple framework for understanding the universality of the maximum drag reduction asymptote in turbulent flow of polymer solutions," *Phys. Rev. E* **92**, 043014 (2015).
- Lockwood, A. P., Peakall, J., Warren, N. J., Randall, G., Barnes, M., Harbottle, D., and Hunter, T. N., "Structure and sedimentation characterisation of sheared $Mg(OH)_2$ suspensions flocculated with anionic polymers," *Chem. Eng. Sci.* **231**, 116274 (2021).
- Lumley, J. L., "Drag reduction by additives," *Annu. Rev. Fluid Mech.* **1**, 367–384 (1969).
- Lumley, J. L., "Drag reduction in turbulent flow by polymer additives," *J. Polym. Sci.: Macromol. Rev.* **7**, 263–290 (1973).
- Lumley, J. L., "Drag reduction in two phase and polymer flows," *Phys. Fluids* **20**, S64–S71 (1977).
- Lumley, J. L., "Coherent structures in turbulence," *Transition and Turbulence* (Elsevier, 1981), pp. 215–242.
- Metzner, A. B., "Polymer solution and fiber suspension rheology and their relationship to turbulent drag reduction," *Phys. Fluids* **20**, S145–S149 (1977).
- Mortimer, L. F., and Fairweather, M., "Density ratio effects on the topology of coherent turbulent structures in two-way coupled particle-laden channel flows," *Phys. Fluids* **32**, 103302 (2020).
- Mortimer, L. F., Njobuenwu, D. O., and Fairweather, M., "Near-wall dynamics of inertial particles in dilute turbulent channel flows," *Phys. Fluids* **31**, 063302 (2019).
- Moser, R. D., Kim, J., and Mansour, N. N., "Direct numerical simulation of turbulent channel flow up to $Re_\tau = 590$," *Phys. Fluids* **11**, 943–945 (1999).
- Nieuwstadt, F., and Den Toonder, J., "Drag reduction by additives: A review" *Turbulence Structure and Modulation* (Springer, 2001), pp. 269–316.
- Oldaker, D., and Tiederman, W., "Spatial structure of the viscous sublayer in drag-reducing channel flows," *Phys. Fluids* **20**, S133–S144 (1977).
- Öttinger, H. C., *Stochastic Processes in Polymeric Fluids: Tools and Examples for Developing Simulation Algorithms* (Springer Science and Business Media, 2012).
- Owolabi, B. E., Dennis, D. J., and Poole, R. J., "Turbulent drag reduction by polymer additives in parallel-shear flows," *J. Fluid Mech.* **827**, R4 (2017).
- Patera, A. T., "A spectral element method for fluid dynamics: Laminar flow in a channel expansion," *J. Comput. Phys.* **54**, 468–488 (1984).
- Peterlin, A., "Molecular model of drag reduction by polymer solutes," *Nature* **227**, 598–599 (1970).
- Pinho, F. T., and Whitelaw, J. H., "Flow of non-Newtonian fluids in a pipe," *J. Non-Newtonian Fluid Mech.* **34**, 129–144 (1990).
- Pope, S. B., *Turbulent Flows* (Cambridge University Press, 2000).
- Sadanandan, B., and Sureshkumar, R., "Viscoelastic effects on the stability of wall-bounded shear flows," *Phys. Fluids* **14**, 41–48 (2002).
- Seyer, F. A., and Metzner, A., "Turbulence phenomena in drag reducing systems," *AIChE J.* **15**, 426–434 (1969).
- Sher, I., and Hetsroni, G., "A mechanistic model of turbulent drag reduction by additives," *Chem. Eng. Sci.* **63**, 1771–1778 (2008).
- Stone, P. A., and Graham, M. D., "Polymer dynamics in a model of the turbulent buffer layer," *Phys. Fluids* **15**, 1247–1256 (2003).
- Sureshkumar, R., "Local linear stability characteristics of viscoelastic periodic channel flow," *J. Non-Newtonian Fluid Mech.* **97**, 125–148 (2001).
- Sureshkumar, R., Beris, A. N., and Handler, R. A., "Direct numerical simulation of the turbulent channel flow of a polymer solution," *Phys. Fluids* **9**, 743–755 (1997).
- Tabor, M., and De Gennes, P., "A cascade theory of drag reduction," *Europhys. Lett.* **2**, 519 (1986).
- Teng, H., Liu, N., Lu, X., and Khomami, B., "Turbulent drag reduction in plane couette flow with polymer additives: A direct numerical simulation study," *J. Fluid Mech.* **846**, 482–507 (2018).
- Thais, L., Gatski, T. B., and Mompean, G., "Analysis of polymer drag reduction mechanisms from energy budgets," *Int. J. Heat Fluid Flow* **43**, 52–61 (2013).
- Tiederman, W. G., Luchik, T. S., and Bogard, D., "Wall-layer structure and drag reduction," *J. Fluid Mech.* **156**, 419–437 (1985).
- Toms, B. A., "Some observations on the flow of linear polymer solutions through straight tubes at large Reynolds numbers," in Proceedings of the International Congress of Rheology (1948).
- Virk, P. S., "Drag reduction fundamentals," *AIChE J.* **21**, 625–656 (1975).
- Vreman, A. W., and Kuerten, J. G. M., "Statistics of spatial derivatives of velocity and pressure in turbulent channel flow," *Phys. Fluids* **26**, 085103 (2014).
- Wedgewood, L. E., and Öttinger, H. C., "A model of dilute polymer solutions with hydrodynamic interaction and finite extensibility. II. Shear flows," *J. Non-Newtonian Fluid Mech.* **27**, 245–264 (1988).
- Wei, T., and Willmarth, W., "Modifying turbulent structure with drag-reducing polymer additives in turbulent channel flows," *J. Fluid Mech.* **245**, 619–641 (1992).
- White, C. M., and Mungal, M. G., "Mechanics and prediction of turbulent drag reduction with polymer additives," *Annu. Rev. Fluid Mech.* **40**, 235–256 (2008).
- Xi, L., "Turbulent drag reduction by polymer additives: Fundamentals and recent advances," *Phys. Fluids* **31**, 121302 (2019).
- Xi, L., and Graham, M. D., "Turbulent drag reduction and multistage transitions in viscoelastic minimal flow units," *J. Fluid Mech.* **647**, 421–452 (2010).
- Yusuf, N., Al-Wahaibi, T., Al-Wahaibi, Y., Al-Ajmi, A., Al-Hashmi, A., Olawale, A., and Mohammed, I., "Experimental study on the effect of drag reducing polymer on flow patterns and drag reduction in a horizontal oil-water flow," *Int. J. Heat Fluid Flow* **37**, 74–80 (2012).